The ICON Earth System Model Version 1.0 1

Johann Jungclaus[1], S J Lorenz[1], H Schmidt[1], V Brovkin[1], N Brüggemann[2], F Chegini[1], T Crüger[1], P De-Vrese[1], V Gayler[1], M A Giorgetta[1], O Gutjahr[2], H Haak[1], S Hagemann[3], M Hanke[4], T Ilyina[1], P Korn[1], J Kröger[1], L Linardakis[1], C Mehlmann[1], U Mikolajewicz[1], W A Müller[1], J E M S Nabel[1], D Notz[2], H Pohlmann[5], D A Putrasahan[1], T Raddatz[1], L Ramme[1], R Redler[1], C H Reick[1], T Riddick[1], T Sam[1], R Schneck[1], R Schnur[1], M Schupfner[4], J.-S Von Storch[1], F Wachsmann[4], K.-H Wieners[1], F Ziemen[4], B Stevens[1], J Marotzke[2], and M Claussen[2]

[1]Max Planck Institute for Meteorology
[2]Universität Hamburg
[3]Helmholtz Zentrum Hereon
[4]DKRZ
[5]Deutscher Wetterdienst

November 23, 2022

Posted on 23 Nov 2022 — CC-BY-NC 4 — https://doi.org/10.1002/essoar.10510175.1 — This a preprint and has not been peer reviewed. Data may be preliminary.

Abstract

* This work documents ICON-ESM 1.0, the first version of a coupled model based 19 on the ICON framework 20 * Performance of ICON-ESM is assessed by means of CMIP6 DECK experiments 21 at standard CMIP-type resolution 22 * ICON-ESM reproduces the observed temperature evolution. Biases in clouds, winds, 23 sea-ice, and ocean properties are larger than in MPI-ESM. Abstract 25 This work documents the ICON-Earth System Model (ICON-ESM V1.0), the first cou-26 pled model based on the ICON (ICOsahedral Non-hydrostatic) framework with its un-27 structured, icosahedral grid concept. The ICON-A atmosphere uses a nonhydrostatic dy-28 namical core and the ocean model ICON-O builds on the same ICON infrastructure, but 29 applies the Boussinesq and hydrostatic approximation and includes a sea-ice model. The 30 ICON-Land module provides a new framework for the modelling of land processes and 31 the terrestrial carbon cycle. The oceanic carbon cycle and biogeochemistry are repre-32 sented by the Hamburg Ocean Carbon Cycle module. We describe the tuning and spin-33 up of a base-line version at a resolution typical for models participating in the Coupled 34 Model Intercomparison Project (CMIP). The performance of ICON-ESM is assessed by 35 means of a set of standard CMIP6 simulations. Achievements are well-balanced top-of-36 atmosphere radiation, stable key climate quantities in the control simulation, and a good 37 representation of the historical surface temperature evolution. The model has overall bi-38 ases, which are comparable to those of other CMIP models, but ICON-ESM performs 39 less well than its predecessor, the Max Planck Institute Earth System Model. Problem-40 atic biases are diagnosed in ICON-ESM in the vertical cloud distribution and the mean 41 zonal wind field. In the ocean, sub-surface temperature and salinity biases are of con-42 cern as is a too strong seasonal cycle of the sea-ice cover in both hemispheres. ICON-43 ESM V1.0 serves as a basis for further developments that will take advantage of ICON-44 specific properties such as spatially varying resolution, and configurations at very high 45 resolution. 46 Plain Language Summary 47 ICON-ESM is a completely new coupled climate and earth system model that ap-48 plies novel design principles and numerical techniques. The atmosphere model applies 49 a non-hydrostatic dynamical core, both atmosphere and ocean models apply unstruc-50 tured meshes, and the model is adapted for high-performance computing systems. This 51 article describes how the component models for atmosphere, land, and ocean are cou-52 pled together and how we achieve a stable climate by setting certain tuning parameters 53 and performing sensitivity experiments. We evaluate the performance of our new model 54 by running a set of experiments under pre-industrial and historical climate conditions 55 as well as a set of idealized greenhouse-gas-increase experiments. These experiments were 56 designed by the Coupled Model Intercomparison Project (CMIP) and allow us to

com-57 pare the results to those from other CMIP models and the predecessor of our model, the 58 Max Planck Institute for Meteorology Earth System Model. While we diagnose overall 59 satisfactory performance, we find that ICON-ESM features somewhat larger biases in 60 several quantities compared to its predecessor at comparable grid resolution. We empha-61 size that the present configuration serves as a basis from where future development steps 62 will open up new perspectives in earth system modelling. 63

Posted on 23 Nov 2022 — CC-BY-NC 4 — https://doi.org/10.1002/essoar.10510175.1 — This a preprint and has not been peer reviewed. Data may be preliminary.

The ICON Earth System Model Version 1.0

J.H. Jungclaus[1], S.J. Lorenz[1], H. Schmidt[1], V. Brovkin[1,6], N. Brüggemann[1,2], F. Chegini[1], T. Crüger[1], P. De-Vrese[1], V. Gayler[1], M.A. Giorgetta[1], O. Gutjahr[1,2], H. Haak[1], S. Hagemann[5], M. Hanke[3], T. Ilyina[1], P. Korn[1], J. Kröger[1], L. Linardakis[1], C. Mehlmann[1], U. Mikolajewicz[1], W.A. Müller[1], J.E.M.S Nabel[1,*], D. Notz[2,1], H. Pohlmann[1,4], D.A. Putrasahan[1], T. Raddatz[1], L. Ramme[1,7], R. Redler[1], C.H. Reick[1], T. Riddick[1], T. Sam[1], R. Schneck[1], R. Schnur[1], M. Schupfner[3], J.-S. von Storch[1,6], F. Wachsmann[3], K.-H. Wieners[1], F. Ziemen[1,3], B. Stevens[1], J. Marotzke[1,6], and M. Claussen[1,6]

[1]Max-Planck-Institute for Meteorology, Hamburg, Germany
[2]Institute of Oceanography, Universität Hamburg, Hamburg, Germany
[3]Deutsches Klimarechenzentrum, Hamburg, Germany
[4]Deutscher Wetterdienst, Hamburg, Germany
[5]Helmholtz Zentrum Hereon, Geesthacht, Germany
[6]Center for Earth System Research and Sustainability (CEN), Universität Hamburg, Germany
[7]International Max Planck Research School on Earth System Modelling, Hamburg, Germany
[*]now at: Max Planck Institute for Biogeochemistry, Jena, Germany

Key Points:

- This work documents ICON-ESM 1.0, the first version of a coupled model based on the ICON framework
- Performance of ICON-ESM is assessed by means of CMIP6 DECK experiments at standard CMIP-type resolution
- ICON-ESM reproduces the observed temperature evolution. Biases in clouds, winds, sea-ice, and ocean properties are larger than in MPI-ESM.

Corresponding author: Johann Jungclaus, `johann.jungclaus@mpimet.mpg.de`

Abstract

This work documents the ICON-Earth System Model (ICON-ESM V1.0), the first coupled model based on the ICON (ICOsahedral Non-hydrostatic) framework with its unstructured, icosahedral grid concept. The ICON-A atmosphere uses a nonhydrostatic dynamical core and the ocean model ICON-O builds on the same ICON infrastructure, but applies the Boussinesq and hydrostatic approximation and includes a sea-ice model. The ICON-Land module provides a new framework for the modelling of land processes and the terrestrial carbon cycle. The oceanic carbon cycle and biogeochemistry are represented by the Hamburg Ocean Carbon Cycle module. We describe the tuning and spin-up of a base-line version at a resolution typical for models participating in the Coupled Model Intercomparison Project (CMIP). The performance of ICON-ESM is assessed by means of a set of standard CMIP6 simulations. Achievements are well-balanced top-of-atmosphere radiation, stable key climate quantities in the control simulation, and a good representation of the historical surface temperature evolution. The model has overall biases, which are comparable to those of other CMIP models, but ICON-ESM performs less well than its predecessor, the Max Planck Institute Earth System Model. Problematic biases are diagnosed in ICON-ESM in the vertical cloud distribution and the mean zonal wind field. In the ocean, sub-surface temperature and salinity biases are of concern as is a too strong seasonal cycle of the sea-ice cover in both hemispheres. ICON-ESM V1.0 serves as a basis for further developments that will take advantage of ICON-specific properties such as spatially varying resolution, and configurations at very high resolution.

Plain Language Summary

ICON-ESM is a completely new coupled climate and earth system model that applies novel design principles and numerical techniques. The atmosphere model applies a non-hydrostatic dynamical core, both atmosphere and ocean models apply unstructured meshes, and the model is adapted for high-performance computing systems. This article describes how the component models for atmosphere, land, and ocean are coupled together and how we achieve a stable climate by setting certain tuning parameters and performing sensitivity experiments. We evaluate the performance of our new model by running a set of experiments under pre-industrial and historical climate conditions as well as a set of idealized greenhouse-gas-increase experiments. These experiments were designed by the Coupled Model Intercomparison Project (CMIP) and allow us to compare the results to those from other CMIP models and the predecessor of our model, the Max Planck Institute for Meteorology Earth System Model. While we diagnose overall satisfactory performance, we find that ICON-ESM features somewhat larger biases in several quantities compared to its predecessor at comparable grid resolution. We emphasize that the present configuration serves as a basis from where future development steps will open up new perspectives in earth system modelling.

1 Introduction

ICON-ESM (V1.0) is the first release of the ICOsahedral Non-hydrostatic Earth System Model that is developed at the Max Planck Institute for Meteorology (MPI-M). It is based on the ICON framework, a joint development of MPI-M, the German Weather Service (Deutscher Wetterdienst, DWD), the Karlsruhe Institute for Technology, and other partner institutions in Germany and Switzerland. It should be noted that the non-hydrostatic part is currently only applicable to the atmospheric component. ICON-ESM combines the ocean ICON-O (Korn, 2017) and atmosphere ICON-A (Giorgetta et al., 2018) components of the ICON modelling system together with ICON-Land, including the Jena Scheme for Biosphere-Atmosphere Coupling in Hamburg JSBACH 4, a complete re-write of the land model JSBACH 3 (Reick et al., 2021, 2013), and the ocean biogeochemistry

module Hamburg Ocean Carbon Cycle (HAMOCC6) (Ilyina et al., 2013). The ocean and atmosphere are coupled using the newly developed coupling software Yet Another Coupler (YAC; Hanke et al., 2016).

At MPI-M, ICON-ESM succeeds the well-established Max Planck Institute for Meteorology Earth System Model (MPI-ESM; Mauritsen et al., 2019) with its component models for the atmosphere European Center Hamburg Model (ECHAM6) (Stevens et al., 2013) and the Max Planck Institute Ocean Model (MPIOM) (Jungclaus et al., 2013), the land model JSBACH 3 (Reick et al., 2013, 2021), and the ocean biogeochemistry module HAMOCC6 (Ilyina et al., 2013). Together with its predecessors, MPI-ESM1.2 has represented three decades of successful model development (see Mauritsen and Roeckner (2020)). The development of a completely new model system is an answer to the requirement for increasing resolution, the need for conservation for the representation of chemical tracers in the atmosphere, and for appropriate scalability on high-performance computers (HPC).

In general, the development of ocean and atmosphere models has taken innovative approaches in the last two decades regarding numerical algorithms, the grid lay-out, and the adaptation to high-performance computing systems. While previous generations of atmosphere models employed mainly spectral transform models, many new developments, in particular those aiming at very high spatial resolution, moved to grid-point methods. The advantages of the latter are more effective data communication (Staniforth & Thuburn, 2011), higher efficiencies at very high resolution (e.g., Satoh et al. (2014); Wedi (2014)), and quasi-homogeneous resolutions avoiding the overly strong grid-size convergence near the poles (Staniforth & Thuburn, 2011). Prominent examples of this new class of models are the Non-hydrostatic Icosahedral Atmospheric Model (NICAM, Satoh et al. (2014)) launched by the Japan Agency for Marine Earth Science and Technology, and the Model for Prediction across scales (MPAS) first developed at the National Center for Atmospheric Research (Skamarock et al., 2012). An overview on dynamical core development is given in Ullrich et al. (2017). In ocean models, unstructured grids provide flexibility with respect to resolving the geometry of the basins and allow for highly varying resolution distribution (Danilov, 2013). Applications of these novel models include regionalized settings realized in The Unstructured Grid Finite Volume Community Ocean Model (FVCOM, Chen et al. (2003)), and global configurations with highly varying resolution using the Finite-Element/volumE Sea ice-Ocean Model (FESOM) (Sein et al., 2017; Scholz et al., 2019), and the MPAS ocean model (Petersen et al., 2019). Formulations on unstructured meshes also face difficulties, e.g., spurious modes or generally higher costs per degree of freedom (Staniforth & Thuburn, 2011; Danilov, 2013), but progress in recent years has proposed solutions (e.g., with respect to spurious modes in Korn and Danilov (2017)), and (component) models based on unstructured grids are now used in CMIP6 climate simulations (Golaz et al., 2019; Semmler et al., 2020).

While the innovative properties of ICON-ESM will be most beneficial in very high-resolution coupled configurations, we present here, as a first step to introduce ICON-ESM to the scientific community, the physical model at a resolution that can be called "standard" in the context of climate simulations for the ongoing Coupled Model Intercomparison Project (CMIP6, Eyring et al. (2016)). We describe a set-up with 158 km grid spacing in ICON-A and 40 km in ICON-O. Focusing on typical climate change experiments, i.e. at least century-long simulations with parameterized physics, the set-up described here offers an efficient configuration for simulations of past, present and future climates, and large ensembles. It also forms the basis for higher-resolution versions as well as for configurations using specific properties of the ICON system, for example grid refinement in ICON-O (Logemann et al., 2021) or nesting in ICON-A (Klocke et al., 2017). In this manuscript, we present the first results of ICON-ESM and provide an examination of the model characteristics in a set of experiments following the CMIP6 Diagnosis, Evaluation, and Characterization of Klima (DECK) protocol and include an ensem-

ble of five CMIP6 "historical" simulations (Eyring et al., 2016). We compare and evaluate the simulations with observations and reanalysis data as well as other models participating in CMIP6 and MPI-ESM.

Typically, model tuning happens initially at the component model level, such as on ICON-A (Giorgetta et al., 2018) and on ICON-O (Korn P. et al., "ICON-O: The ocean component of the ICON Earth System Model - global simulation characteristics and local telescoping capability", manuscript submitted to JAMES, Korn22 hereafter). Coupled together, these completely new ICON components for ocean, sea-ice, land and atmosphere repeatedly revealed unexpected behavior that required detailed investigations and major tuning efforts, which we partly describe in this manuscript (section 3). In the following, we provide information on the general circulation models for atmosphere and ocean, the sea-ice model, the ocean biogeochemistry module, the land model, and the coupler. Then we describe the spin-up and tuning of the coupled system that has led to the pre-industrial control simulation (piControl) under constant forcing agents. Evaluation in comparison with observations and reanalyses data is based on the last decades of a small ensemble of CMIP6 historical simulations and the model's climate sensitivity characteristics are assessed in idealized global warming experiments (i.e., the 1 %CO_2 yr^{-1} increase experiment (1pctCO2) and the experiment with an abrupt four-fold CO_2 concentration (abrupt4xCO2)). We discuss tuning choices in section 5 and end with a summary and conclusion (section 6).

2 Model overview

The ICON model system (Zängl et al., 2015) provides common infrastructure (e.g. grid construction and output handling) and, in part, common numerical operators for the component models. A common feature is the basic grid construction based on unstructured, icosahedral grids. The grids for both the ICON-A and ICON-O model are created by recursively dividing the original twenty triangles of the icosahedron. This is done by bisecting the edges (Figure 1b). The vertices at each step are projected at the Earth sphere. The primary cells are triangles, while the dual cells are hexagons, except for the original twelve pentagons of the icosahedron which remain. A detailed description of the process is given in H. Wan et al. (2013) and Giorgetta et al. (2018). The spring dynamics grid optimization is applied on both grids. This is a grid optimization process that aims to smooth the grid in order to improve the numerical behavior of the model (see Tomita et al. (2001) and Tomita et al. (2002)). The grids are symmetrized with respect to the equator by reflecting the northern hemisphere to the south. The equatorial-symmetric grid has been tested with the ICON-O for shallow water set-ups and showed reduced errors (Korn & Linardakis, 2018). Local asymmetries in grids can be the cause of increased numerical errors (Weller et al., 2009). For the icosahedron, these asymmetries occur most profoundly in the vicinity of the pentagons (Korn & Linardakis, 2018). It is desirable to keep these "hot" spots away from areas where large velocities may occur, for example due to the orography. Therefore the grid was rotated 37^o eastwards, to avoid placing a pentagon over the Himalaya region. In the set-up presented here, the resolution for the ICON-A grid is 158 km, measured as the square root of the average triangle area, with a total of 20480 triangles (the R2B4 grid in Table 1 of Giorgetta et al. (2018)). The ICON-O grid has an average resolution of 40 km and 235403 triangles, the land triangles being removed to reduce memory and computing resources. The choices for horizontal and vertical resolutions reflect necessities for efficiently running the set-up for hundreds or thousands of years. The atmosphere's horizontal resolution is comparable to the T63 version of MPI-ESM-LR (Mauritsen et al., 2019) and the ocean's globally uniform resolution of 40km is close to the "TP04" grid used in MPI-ESM-HR (Müller et al., 2018). The 40 km ocean resolution is barely "eddy permitting", but allows for passages and straits to be adequately resolved.

The bathymetry was interpolated from the Shuttle Radar Topography Mission (SRTM) 3 PLUS dataset (Becker et al., 2009), adjusted to conform with the sea-land mask given by the Global Land Cover Characterization (GLCC) 2.0 dataset (GLCC, 2018)). The ICON-O sea-land mask is then projected to the coarser ICON-A grid, allowing for triangles to be partially ocean.

The numerical schemes of the atmosphere and the ocean share commonalities but feature also significant differences. Identical in both components is the spatial discretization of differential operators such as divergence and curl through mimetic methods (cf. Korn (2017)). This takes advantage of identical grid structures and the Arakawa-C-type staggering of variables. The staggering necessitates reconstructions and interpolations to connect variables that are located at different grid positions to calculate fluxes. This is accomplished in ICON-O by the novel concept of *Hilbert space admissible reconstructions* (for details see Korn (2017), Korn and Linardakis (2018)). The development of the atmosphere's dynamical core required different choices and therefore ICON-A relies on several interpolation methods (see Zängl et al. (2015)).

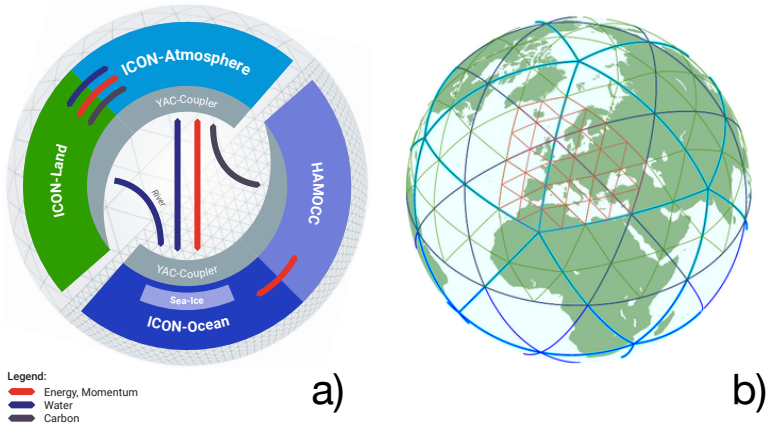

Figure 1. Schematic representation of the model components of the ICON-ESM (a) and the construction of the grid through the bisection process (b).

2.1 Atmosphere

The atmosphere component of the ICON-ESM is the icosahedral nonhydrostatic atmospheric general circulation model ICON-A. The model version used here is similar to version 1.3.00 described in detail by Giorgetta et al. (2018), which was evaluated by Crueger et al. (2018). Modifications with respect to this earlier version are described below. The dynamical core of the model (Zängl et al., 2015) and the transport scheme are shared with a configuration used for numerical weather prediction (NWP) at the DWD. Other variants of the ICON atmosphere model include the option to interactively couple to the Aerosol and Reactive Trace gases scheme ART (Rieger et al., 2015) and a configuration including the upper atmosphere (UA-ICON, Borchert et al., 2019). The ICON-A descretization is based on an Arakawa-C grid finite difference approach, which provides better scaling behavior compared to the spectral method utilized by the previous ECHAM atmosphere model. These superior scaling capabilities of ICON have enabled global storm-resolving simulations down to a horizontal grid resolution of about 2.5 km (Stevens et al., 2019).

The model configuration used here differs from the NWP variant in particular with respect to the physics package, which was adopted from the ECHAM6 general circula-

tion model (Stevens et al., 2013) used in the MPI-ESM (Giorgetta et al., 2013; Mauritsen et al., 2019). The physics parameterizations include the PSrad radiation scheme of Pincus and Stevens (2013), a scheme for turbulent vertical diffusion based on a total turbulent energy approach as proposed by Mauritsen et al. (2007), a convection parameterization based originally on the Tiedtke (1989) mass flux scheme, a parameterization for the representation of stratiform clouds including microphysics based on a scheme by U. Lohmann and Roeckner (1996) and cloud cover diagnosed following Sundqvist et al. (1989), a representation of the effects of gravity waves and blocking from sub-grid scale orography following Lott (1999), and the Hines (1997) parameterization of the effects of non-orographic gravity waves. Adaptations of the original ECHAM parameterization schemes for the use in ICON-A are described by Giorgetta et al. (2018). As in the latter publication, we use ICON-A here with a horizontal grid resolution of 158 km. In the vertical, the model employs a terrain following hybrid sigma-height grid with 47 layers extending to a model lid at 83 km. The lowermost layer has a thickness of 40 m. In total 6 layers cover the altitude range up to about 1 km, 23 layers up to about 16 km, and 39 layers up to about 50 km. Also the prescription of solar irradiance, radiatively active trace gases, and aerosols is unchanged with respect to the description provided by Giorgetta et al. (2018).

Compared to the ICON-A version 1.3.00 described by Giorgetta et al. (2018) the following modifications have been made. (A) The coupling of the physical processes has been serialized completely using the following sequence: (1) radiative effects by terrestrial longwave and solar shortwave radiation, (2) vertical diffusion with implicitly coupled land surface processes, (3) non-orographic gravity wave drag, (4) subgrid-scale orographic (SSO) effects, (5) cumulus convection, and (6) cloud microphysics. This improved the numerical stability and allowed to increase the model time step from 10 to 15 minutes. Furthermore, the time step for radiation, the only process not computed at every model time step, was shortened from 120 to 90 minutes. (B) The non-orographic gravity wave and SSO effects were re-tuned. Here, new SSO parameters for the statistical description of the unresolved terrain were used, which resolve both issues discussed in section 4.7.1 of Giorgetta et al. (2018), i.e. the error in the azimuthal angle of the unresolved mountains, and the standard deviation of unresolved orographic height, which is now computed with respect to the resolved sloped terrain. Additionally, a weighting factor for the non-ocean fraction has been introduced to account for the fact that the SSO parameters are computed for the area fraction that is land or lake or glacier, i.e. non-oceanic. (C) The physical processes were re-tuned for a balanced top-of-atmosphere (TOA) radiation and in order to minimize the systematic errors in Atmosphere Model Intercomparison Project (AMIP) simulations.

In step (B), tuning parameters *gkdrag*, which scales the magnitude of the orographic gravity wave drag, and *gkwake*, which scales the blocking of low-level flow by unresolved orography, were tested with values in the range of 0.01 to 1 with the following goals: The first target was to reduce the systematic error in zonal mean zonal wind in boreal winter (December, January, February, DJF) at 60^o N at 10 hPa. The secondary target was then to minimize errors in the zonal mean zonal wind in boreal summer (June, July, August, JJA) as well as errors in annual mean pressure at sea level and annual mean zonal wind stress at the ocean surface. This led to new default parameters $gkdrag = 0.05$ and $gkwake = 0.05$, instead of $gkdrag = 0.10$ and $gkwake = 0.01$ (Giorgetta et al., 2018). The tuning parameters for the non-orographic gravity wave drag remained as in Giorgetta et al. (2018).

In step (C) a range of tests was conducted with modifications in tuning parameters for fractional cloud cover, entrainment of environmental air in convective plumes, overshooting mass flux fraction at the top of convection, and cloud microphyiscs. From all tests a configuration with three modifications was chosen, compared to Giorgetta et al. (2018): The entrainment coefficients for deep and shallow convection were set to *entrscv* =

entrpen = 0.0003 m^{-1} (compared to *entrscv* = 0.003 m^{-1} and *entrpen* = 0.0002 m^{-1}), and the convective mass flux fraction across the level of neutral buoyancy at the top of convection was reduced to *cmfctop* = 0.1 (compared to *cmfctop* = 0.2). The critical relative humidities for condensation near the surface (*crs*) and in the upper troposphere (*crt*) were kept unchanged. This configuration performed best following a similar evaluation as presented in Giorgetta et al. (2018). However, it should be noted that other tested configurations were equally acceptable concerning the radiation balance at the top of the atmosphere, which was the primary tuning goal.

The resulting atmospheric model configuration provided the starting point for the development of the coupled model system in the pre-industrial control experiment, which lead to additional changes of tuning parameters for dynamics as well as physics, as described in Section 3 and reviewed in the discussion section.

2.2 Ocean

ICON-O, the ocean general circulation model that provides the ocean component of ICON-ESM, solves the hydrostatic Boussinesq equations. These dynamical equations are also referred to as the "primitive equations". The state vector consists of horizontal velocity, the oceanic tracers potential temperature and salinity, as well as the surface elevation. The primitive equations are solved on the triangular ICON grid with an Arakawa C-type staggering that places tracers at the circumcenter of a triangular cell and the normal component of the velocity vector at the midpoint of the cells edge. The vertical coordinate-axis is given by the z-coordinate (or geopotential height). The two-dimensional triangles are simply extended by a height-based dimension. This generates three-dimensional prisms. The number of vertical levels depends on the topography and varies from cell to cell $N_z = N_z(K)$. The grid used here applies 64 vertical levels with spacing varying between 10 m in the upper 100 m and 250 m in the deep ocean. The level thickness is constant in time, except for the surface layer with its varying sea surface elevation. The latter and the varying sea-ice draft dictates limits for the allowed "thinness" of the surface layer. To overcome this limitation, we are presently implementing the z* coordinate, where the vertical coordinate is scaled in proportion with the sea-surface elevation (Adcroft & Campin, 2004).

The subgrid scale closure for velocity uses a biharmonic operator based on the vector Laplacian with a viscosity coefficient that scales with the square root of edge length times cell center distance to the third power. Eddy-induced diffusion and eddy-induced advection are parameterized following Redi (Redi, 1982) and Gent-McWilliams (GM) (P. Gent & McWilliams, 1990), respectively. We employ the variational approach of S. Griffies et al. (1998) and S. Griffies (1998). The discretization of the variational approach is, however, different from the triad approach of S. Griffies et al. (1998) and uses inherently unstructured grid methods. The Hilbert-space-compatible reconstructions and mimetic differential operators of ICON-O's dynamical core provide a discrete Hilbert space that allows a direct and structure-preserving discretization of the eddy parameterization. Full details are given in Korn (2018). Since the 40km ocean grid used here is barely eddy-permitting, we keep the GM scheme switched on using a default GM thickness diffusivity parameter κ of 400 $m^2 s^{-1}$, which is constant throughout the water column.

As equations of state that approximates the density as a function of potential temperature, salinity and depth we use the UNESCO-80 formulation. For the parameterization of turbulent vertical mixing, ICON-O offers different choices: a Richardson-number-dependent parameterization (Pacanowski & Philander, 1981) (PP) including an additional wind-mixing formulation as in MPIOM, the KPP scheme (Large et al., 1994), or, as the standard setting used here, a scheme based on a prognostic equation for turbulent kinetic energy (TKE) that implements the closure suggested by Gaspar et al. (1990). In the interior ocean, where vertical mixing is induced by breaking internal waves, the

standard TKE scheme requires a constant value of turbulent kinetic energy, which is set to $10^{-6}m^2s^{-2}$ in the simulations described here. As part of our ongoing development work, the TKE scheme is presently implemented into the Community Vertical Mixing CVMix library (S. M. Griffies et al., 2015; Van Roekel et al., 2018) and extended by the Internal Wave Dissipation Energy and Mixing (IDEMIX) scheme (Olbers & Eden, 2013). IDEMIX describes energy transfers from internal wave sources to sinks and includes the effects of internal tides and near-inertial-wave induced mixing. Further extensions include a parameterization of Langmuir circulation following Axell (2002). Vertical dissipation and vertical diffusion are discretized implicitly. The transport of potential temperature, salinity, and the biogeochemical tracers is accomplished by a flux-corrected transport method with a Zalessak limiter, which utilizes flux calculation by compatible reconstructions (Korn, 2017). The free surface equation is solved implicitly in time with an iterative solver based on the conjugated gradient method. The remaining state variables are discretized explicitly. For details we refer to Korn (2017). ICON-O's time stepping applies a semi-implicit Adams-Bashford-2 scheme. In the present configuration, the ocean's time step is 30 minutes, which is also the frequency of data exchange with the atmosphere.

2.3 Sea Ice

The sea-ice model consists of a dynamic and a thermodynamic component that are called once at every ocean time step. The thermodynamics of the ICON sea-ice code, which describe the freezing and melting of sea ice, have been adopted from MPI-OM (Notz et al., 2013) and employ a single-category, zero-layer formulation (Semtner, 1976). For many climate-scale research questions, this simple setup has proven sufficient in comparison with more complex models (Notz, 2020). The sea-ice dynamics are based on the sea-ice dynamics component of the Finite Element Sea Ice Model (FESIM, Danilov et al., 2016), which uses the standard elastic-viscous-plastic (EVP) formulation. As ICON-O applies an analogue of an Arakawa C-grid and FESIM uses an Arakawa A-grid type staggering, an interpolation between the ICON-O grid and the FESIM sea-ice dynamics is necessary. Furthermore, an additional rotation of the oceanic and atmospheric variables is required, because ICON-O uses local coordinates, whereas FESIM is based on rotated geographic spherical coordinates. Besides the computational overhead, the coupling between FESIM and ICON-O introduces numerical diffusion, e.g. at least three grid cell wide passages are required to allow a sea-ice transport. To overcome those limitations we are currently working on the integration of a newly developed sea ice dynamic model (Mehlmann & Korn, 2021).

2.4 Ocean Biogeochemistry

In ICON-ESM, ocean biogeochemistry is represented by HAMOCC6, which simulates biogeochemical tracers in the water column and in the upper sediment (Ilyina et al., 2013; Paulsen et al., 2017; Mauritsen et al., 2019). In the water column, currently at least 20 biogeochemical tracers are prognostically calculated, generally following an extended nutrient, phytoplankton, zooplankton, and detritus (NPZD) approach, also including dissolved organic matter, as described in Six and Maier-Reimer (1996). The co-limiting nutrients consist of phosphate, nitrate, silicate and iron. A fixed stoichiometry for all organic compounds is considered. Phytoplankton is represented by bulk phytoplankton and diazotrophs (nitrogen fixers; Paulsen et al. (2017)). Particulate organic matter (POM) is produced by zooplankton grazing on bulk phytoplankton and enters the detritus pool. Export production is separated explicitly into $CaCO_3$ and opal particles, each sinking with its own sinking velocity. The POM sinking speed can be assigned using one of the three implemented methods: constant speed, linearly increasing speed with depths below the euphotic zone (also known as the 'Martin curve'; Martin et al. (1987)) or calculated using the recently developed M4AGO scheme (Maerz et al., 2020). The rem-

ineralization of detritus throughout the water column is either aerobic (if seawater oxygen concentration $> 0.5\ \mu molL^{-1}$) or anaerobic by denitrification and sulphate reduction. The upper sediment is resolved by 12 biologically active layers and a burial layer and simulates the dissolution and decomposition of particulate inorganic and organic matter and the diffusion of pore water constituents. The HAMOCC model is also part of the MPI-ESM and has been extensively evaluated in previous single-model, e.g. Ilyina et al. (2013); Paulsen et al. (2017); Müller et al. (2018); Mauritsen et al. (2019); Maerz et al. (2020) and multi-model studies, e.g. Bopp et al. (2013); Kwiatkowski et al. (2020); Séférian et al. (2020).

Within the HAMOCC core subroutines, only the biological and chemical sources and sinks, as well as tracer sinking and ascending are computed. Therefore, when implementing HAMOCC6 (the model version used in MPI-ESM CMIP6 simulations) in ICON-ESM, the HAMOCC6 interface to the ocean and atmosphere components was adjusted to the ICON-ESM infrastructure accordingly. This adjustment includes the transport of biogeochemical tracers with the same routines and numerical schemes as the physical tracers of the ICON-O model. As in previous model versions, it was ensured that all chemical constituents in HAMOCC are mass conserving within computational precision in this implementation.

2.5 Land

ICON-Land is a novel framework developed at MPI-M for the modeling of land processes in ICON that clearly separates model infrastructure from land surface process descriptions. It features a flexible scheme of land surface tiling and object-oriented organization of physical and biogeochemical processes. Apart from the ICON-ESM configuration, ICON-Land is used in the ICON-A atmosphere configuration and can also be run in a land stand-alone mode (see e.g. Nabel et al., 2020). The ICON-Land implementation used in the ICON-ESM v1, comprises physical and biogeochemical processes provided by the JSBACH 4 land model, a port of JSBACH 3.2 (Reick et al., 2021) to the ICON-Land framework. Previous JSBACH versions have represented the land components of the MPI-ESM versions used in CMIP5 (Giorgetta et al., 2013) and CMIP6 (Mauritsen et al., 2019).

Compared to Reick et al. (2021), JSBACH 4 features certain improvements of the physical processes at and below the surface, including a five-layer snow scheme and the phase change of water within the soil (Ekici et al., 2014; de Vrese et al., 2021). Also included are the options to calculate the soil thermophysical properties depending on the soil water content and the general properties depending on the organic matter content of a given soil layer. Surface runoff and sub-surface drainage from ICON grid cells are routed through a hydrologic discharge model (Hagemann & Dümenil, 1997) using a novel method for generating river directions (Riddick, 2021); the resulting river discharge is coupled as freshwater flux to the ocean via the YAC coupler (see section 2.6). Surface temperature of lakes is computed by a simple mixed-layer scheme including ice and snow on lakes (Roeckner et al., 2003). The surface energy balance and the soil thermal layers on land are coupled implicitly to the vertical diffusion scheme of ICON-A.

In the model version discussed in this study, biogeochemical processes in JSBACH 4 are simplified relative to JSBACH 3 (Reick et al., 2021). Natural vegetation dynamics (Brovkin et al., 2009) coupled to land-use transitions (Reick et al., 2021), as well as the coupling of terrestrial carbon and nitrogen cycle (Goll et al., 2017) have not yet been ported from JSBACH 3, but are planned to be ported into future ICON-ESM versions. In the piControl and historical simulation ensemble (section 4), natural vegetation and anthropogenic land cover change have been prescribed by annual maps of cover fractions on 11 Plant Functional Types (PFTs) based on Pongratz et al. (2008) and transient crop

and pasture fractions derived from the land use harmonization (LUH) LUH2 v2h (Hurtt et al., 2019) as described in Mauritsen et al. (2019).

2.6 Coupling

Ocean and atmosphere processes run concurrently. The data exchange between the two horizontal grids is implemented using the Yet Another Coupler (YAC) coupling library (Hanke et al., 2016) in version YAC1.5 (Hanke & Redler, 2019). Fig. 1 depicts a schematic view of the model components and the exchange of coupling fields. The components of the wind- and velocity vectors are interpolated using Bernstein-Bézier polynomials following Liu and Schumaker (1996) to better represent the vorticity. Target cells for which this interpolation method fails due to an incomplete interpolation stencil near land-sea borders are interpolated using a 4-nearest-neighbour arithmetic average interpolation. The river discharge is remapped to the target grid in a way that each source cell containing a river discharge value is assigned to a coastal target cell on the ocean grid. All other fields are interpolated using first-order conservative remapping. To avoid problems with the conservation of the field properties with this method, the grids and masks of the model components are constructed such that any unmasked source cell is always covered by unmasked target cells The weights required for the remapping are calculated by YAC at the start of each run. This calculation is based on the grid information provided by the model.

The atmosphere component provides the zonal and meridional components of the wind-stress separately over ice and over water, the surface fresh water flux as rain and snow over the whole grid cell and evaporation over the ocean fraction of the cell, short- and longwave radiation and latent and sensible heat fluxes over the ocean, sea ice surface and bottom melt potentials, the 10 m wind speed and sea level pressure. The ocean provides the sea surface temperature, the zonal and meridional components of velocity at the sea surface as well as ice- and snow thickness, and ice concentration. The data exchange encompasses aggregation, averaging and re-partitioning of the exchange fields. YAC routines are called at every model time step of the respective model component, and data are accumulated inside the YAC library. The model setup is configured such that every 1,800 seconds, the coupling period, the aggregated data are averaged and sent to the respective receiving processes. This coupling period has to be an integer multiple of the time steps of the model components taking part in this exchange.

2.7 Computational configuration and performance

All simulations were performed with the bullx DLC 720 high performance computing system for Earth system research (HLRE-3) of the "Deutsches Klimarechenzentrum" (DKRZ). The simulations utilize 120 "Broadwell" compute nodes of the system named "Mistral", which include 36 processing units each.

The domain decomposition is performed separately for ocean and atmosphere: the ocean decomposition at 40 km horizontal resolution, which includes only ocean grid points, and the global atmosphere decomposition at 158 km horizontal resolution. The sea-ice model is included in the ocean code and runs on its own FESIM grid (see section 2.3), which is coupled directly to the ICON-O grid. The land model works within the ICON-A decomposition. The YAC coupling library is linked to each of the two components of the ICON model (atmosphere/land and ocean/sea-ice) and performs the aggregation, averaging and re-partitioning of the exchange fields using their respective decomposition.

Due to this technical setup, the load balancing has to be optimized for these two major components, only. The heavy workload due to multiple tracers in configurations with HAMOCC requires different weightings for run with and without ocean biogeochemistry. The best compromise between shortest return time and parallelization overhead

was obtained for a load balancing of 74 nodes (2664 mpi-processes) for running ocean and sea-ice (without HAMOCC) on the 40 km grid and concurrently using 46 nodes (1656 mpi-processes) for atmosphere and land on the 158 km grid. With this configuration we achieve an average performance of ten simulation years in one batch-job executing within roughly two hours. Without any queuing-time at the machine (depending on the load of the machine, or by assigning high-priority to the job-chain) it results in a performance of up-to 120 simulated years per day. A hybrid configuration using mpi- as well as openmp- (shared memory) parallelization was tested and exhibited less performance on the DKRZ machine, which is probably due to partly missing optimizations in the code. In the runs including HAMOCC, the best optimization was achieved for a load balancing of 46 nodes for atmosphere and land and 154 nodes for the ocean (physics and biogeochemistry) and sea ice. An average performance of 40 simulated years per day was achieved with this configuration.

3 Tuning and spin-up

3.1 Tuning principles and targets

Model tuning is an integral part of the model development process (Mauritsen et al., 2012). Since there are many similarities between ICON-ESM and MPI-ESM regarding physical parameterizations and the sea-ice thermodynamics, the tuning process profited from several generations of MPI-ESM development (Mauritsen et al., 2012, 2019; Jungclaus et al., 2013; Notz et al., 2013). In the coupled system, a first-order tuning goal is to achieve stable climate conditions to minimize drifts in the piControl climate used as reference for climate change simulations. A near-zero top-of-atmosphere energy-flux balance is required as well as long-term stable circulation, for example the Atlantic Meridional Overturning Circulation (AMOC) in the ocean. Furthermore, it is desired to match the model results with the observed climate conditions for the second half of the 19^{th} century and with the temperature evolution over the 20^{th} century. Based on experience gained in the tuning of the stand-alone ocean and atmosphere set-ups (Giorgetta et al., 2018), a small number of parameters associated with the parameterization of specific processes were selected for tuning (Table 1). In the atmosphere these parameters are mainly related to convection, clouds, and subgrid-scale orographic processes, and largely overlap with parameters used in the tuning of the atmosphere stand-alone model (see Section 2.1). Parameters modified for tuning purposes in the ocean include the coefficient for isoneutral diffusion K and the coefficient for eddy-induced advection κ in the Gent-McWilliams closure (Korn, 2018). Apart from albedo settings in the atmosphere, the sea-ice model contains two main parameters that we use to tune the overall mean state of the sea-ice cover. One of these parameters describes the change in ice-thickness distribution during freezing ($leadclose_1$), and the other parameter describes the change in ice-thickness distribution during melting ($leadclose_2/3$) as described in Notz et al. (2013).

3.2 Spin-up and tuning history

The ocean initial conditions for temperature and salinity were taken from the Polar Science Center Hydrographic Climatology data set PHC 3.0 (Steele et al., 2001). First, a 200-year long stand-alone ICON-O simulation was carried out using the atmospheric climatology forcing and the respective bulk formulae described in Marsland et al. (2003). Starting from the restart fields obtained from the stand-alone ocean simulation, several experiments with different tuning choices were conducted, partly sequentially with parameter changes on the fly, partly in parallel to study difference in drift behavior. The final tuning sequence is documented in Fig. 2.

The start of the coupled simulation (slo1304) is characterized by a large drift, where both atmosphere and ocean are cooling and the TOA radiation balance is negative (2 b). Introducing background tropospheric aerosols in the run slo1307 led to even stronger

Table 1. Parameters used for tuning the coupled model.

ICON Parameter	Symbol	Value	Reference	Description
Atmosphere				
crs	$r_{0,surf}$	0.978	Giorgetta et al. (2018)	critical relative humidity for condensation (surface)
crt	$r_{0,top}$	0.8	Giorgetta et al. (2018)	critical relative humidity for condensation (upper troposphere)
entrpen	ϵ^1	$0.00015m^{-1}$	Nordeng (1994)	entrainment in deep convection
gkdrag	G	0.03	Lott (1999)	subgrid-scale orographic (SSO) gravity wave drag
gkwake	C_d	0.03	Lott (1999)	SSO low-level blocking
gklift	C_1	0.7	Lott (1999)	SSO lifting
Ocean				
K	K	400 m^2s^{-1}	Korn (2018)	Redi isoneutral diffusion
κ	κ	400 m^2s^{-1}	Korn (2018)	GM eddy-induced advection
sea ice				
leadclose 1	cmelt	0.5	Notz et al. (2013)	ice area change during melting
leadclose 2/3	cfreeze	0.666	Notz et al. (2013)	ice area change during freezing

decrease in global mean surface air temperature (GSAT) that required counter-tuning. This was achieved by increasing the critical relative humidities for condensation *crs* and *crt* and the entrainment parameter *entrpen* which led in particular to a reduction of global mean cloud fraction and an increase of net incoming radiation at the TOA. While this resulted initially in overly strong warming, the long-term drift cooled the model to acceptable values and we finally obtained a solution with small overall drift even in the deep ocean (2 c). While this may appear as a very straightforward tuning process, a large number (order 100) of further model experiments with different parameter settings and simulated lengths of a few years to several hundreds of years have been performed to arrive at this spin-up sequence. The influences of some of the tuning choices on the simulated climate are discussed in several parts of the model evaluation of Section 4 and in section 5.

A bug-fix related to erroneous snow accumulation in a few grid points required an update of the code in run slo1325 without noticeable effects on the climate. This simulation was carried out for another 500 years, where we defined the start of the piControl simulation. The starting point of piControl was also used to initialize the DECK experiments 1pctCO2 and abrupt4xCO2, and one realization of the historical simulations. Further realizations were started from different dates of piControl. In addition, an AMIP simulation was included using the same code version as the coupled experiments.

After the completion of the DECK experiments presented in this paper, a coding error was detected in the vertical diffusion of ICON-A. The bug is related to the way ocean currents are taken into account in the wind-stress calculation. The effects of the error turned out to be time-step and grid-size dependent and had detrimental effects in a very high-resolution (5km) coupled proto-type model. At the low resolutions applied here, we were able to identify typical effects of this error (e.g. some changes in the representation of the equatorial current system in the ocean), but most of the analyzes and illustrations presented here remain largely unaffected. The most notable effect is an even stronger variance of the ENSO time series, but we diagnosed otherwise very similar characteristics of the variability (not shown). We have concluded that the bug must be fixed but changes to the results were too minor to justify a repetition of the DECK experiments and their post-processing. All conclusions regarding benefits and shortcomings of the ICON-ESM DECK simulations presented here remain unaffected.

The tuning of the ocean biogeochemistry was carried out after the tuning of the coupled setup. A first-order tuning goal for the ocean biogeochemistry in an ESM is to limit significant drifts in the biogeochemical tracer fields and fluxes in the piControl run.

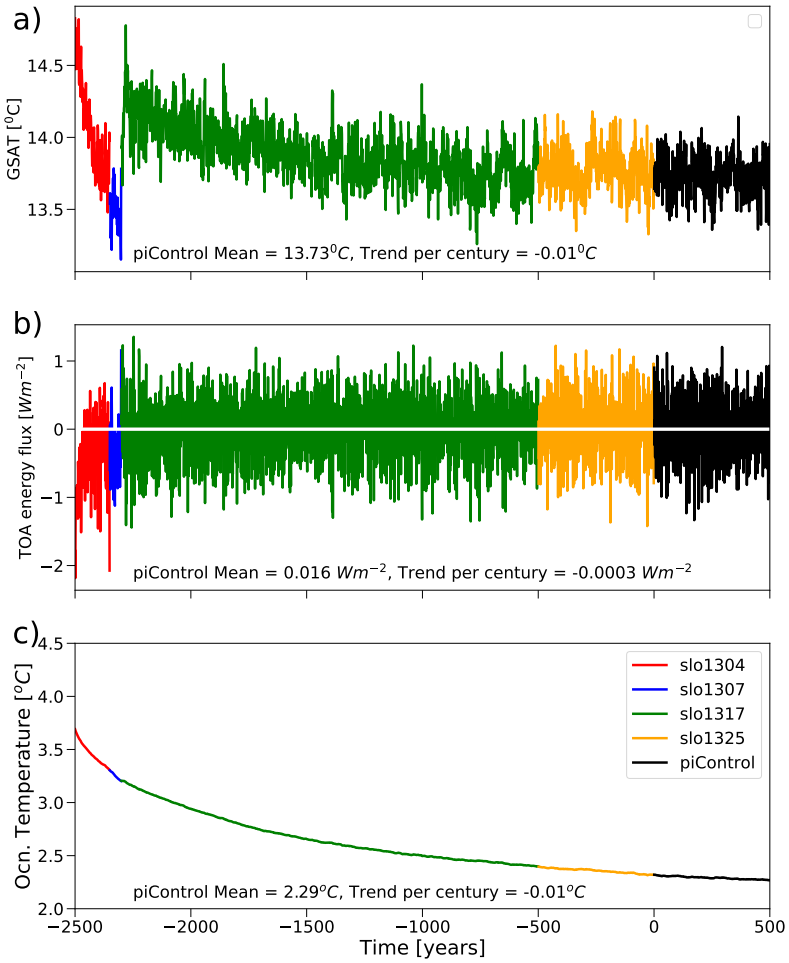

Figure 2. Spin-up history of the coupled simulation: time series of global mean surface air temperature (a), top-of-atmosphere (TOA) radiation flux (b), and volume-averaged ocean temperature (c) evolution from a sequence of simulations leading to the piControl experiment.

Furthermore, parameters are adapted within a reasonable range to drive the model closer to observations. The initial conditions for the biogeochemical tracer fields in the water column and sediment were interpolated from a previously well spun-up MPIOM piControl setup which was run for several thousands of years. Ocean and atmosphere were initialized from the end of the slo1325 run and ICON-ESM was run with the piControl climate. The dust deposition climatology of Mahowald et al. (2005) and historical nitrogen deposition fields from the CMIP6 input database (https://esgf-node.llnl.gov/projects/input4mips/) were used. The POM sinking speed was calculated based on the Martin curve.

To account for the ocean circulation simulated by ICON-ESM, some of the HAMOCC tuning parameters were changed from their default values. For this, first several experiments with different tuning choices were conducted to obtain the approximate values for the tuning parameters. The parameters were then fine tuned on the fly during a simulation length of 450 years. The appropriate weathering rates, which are used to compensate for the loss of carbon and nutrients from the water column to the sediment, were calculated and updated during the simulation. After that, the model was spun-up for 250 years, during which the model was in a semi-steady state in the ocean global monitoring values such as the global surface alkalinity, export from euphotic zone and 1000m,

primary production and nutrients. The simulated annual global flux of CO_2 into the ocean at this state was about 0.05 PgC/yr, representative for the assumption of the pre-industrial steady-state condition.

Table 2. Overview on the ICON-ESM simulations.

Experiment	Description	Period	Ens.size	Initialization
piControl	Preindustrial Control	500 years	1	spin-up run
1pctCO2	idealized CO_2-increase	150 years	1	spin-up run
abrupt4xCO2	idealized CO_2 increase	150 years	1	spin-up run
historical	transient forcing	1850-2014	5	piControl (yrs 0, 100, 200, 300, 400)
AMIP	atmosphere-only	1978-2014	1	n.a.
HAMOCC historical	transient forcing	1850-2014	1	HAMOCC spin-up

4 Model evaluation

The set of experiments described in this paper is listed in table 2. We start with a brief account of the piControl experiment. Since the evaluation in comparison with observations is based on data from the recent decades, we perform the analyzes based on the historical ensemble. The idealized climate change experiments 1pctCO2 and abrupt4xCO2 are used to estimate the climate sensitivity of ICON-ESM in section 4.4.

4.1 The pre-industrial control simulation (piControl)

In Figure 2 we have compiled the temporal evolution of key quantities reflecting the stability of the climate over centuries. The time series include the 500-yr long piControl experiment (black). The GSAT is stable over the 500 year long piControl simulation with a small cooling of -0.01 K per century (Fig. 2 a). A pre-industrial GSAT of 13.73^oC is consistent with the present temperature level based on reanalyses and the observed estimate of global warming over the historical period (Hawkins & Sutton, 2016). The goal of a very stable TOA energy flux is achieved with a small imbalance of 0.016 Wm^{-2} (Fig. 2 b). In contrast, the ocean is still cooling (Fig. 2 c) and the average ocean cooling over the piControl run translates to an energy loss of -0.047 Wm^{-2}, leaving a mismatch of 0.063 Wm^{-2}. This spurious energy loss reflects inconsistencies in the coupling procedure and/or the atmosphere that we are unable to identify at this stage. However, the imbalance is sufficiently small compared to changes in, for example anthropogenic forcing and much smaller than the energy leakages identified in ECHAM6 by Mauritsen et al. (2012).

Figure 3 includes additional integrated measures of the stability of the simulations. The overall sea-ice distributes is sensitive to long-term drift in radiation balance and/or ocean heat transports (Fig. 3 a, b). While Southern Hemisphere summer sea-ice extent is always too close to zero, the remaining time series show multi-decadal variability, but only small long-term drift.

The AMOC (Fig. 3 c) is a key quantity for the meridional heat exchange in the Atlantic Ocean and its stability is important for maintaining a proper sea-ice distribution and North Atlantic deep water formation (for more details see section 4.2.5). The control run has a time-mean AMOC strength at 26^oN of slightly less than 16 Sv ($1Sv = 1Sverdrup = 10^6 m^3 s^{-1}$). The AMOC is stable over the last 1000 years of the simulation, but exhibits relatively strong multi-decadal variations with an amplitude of up to 3 Sv.

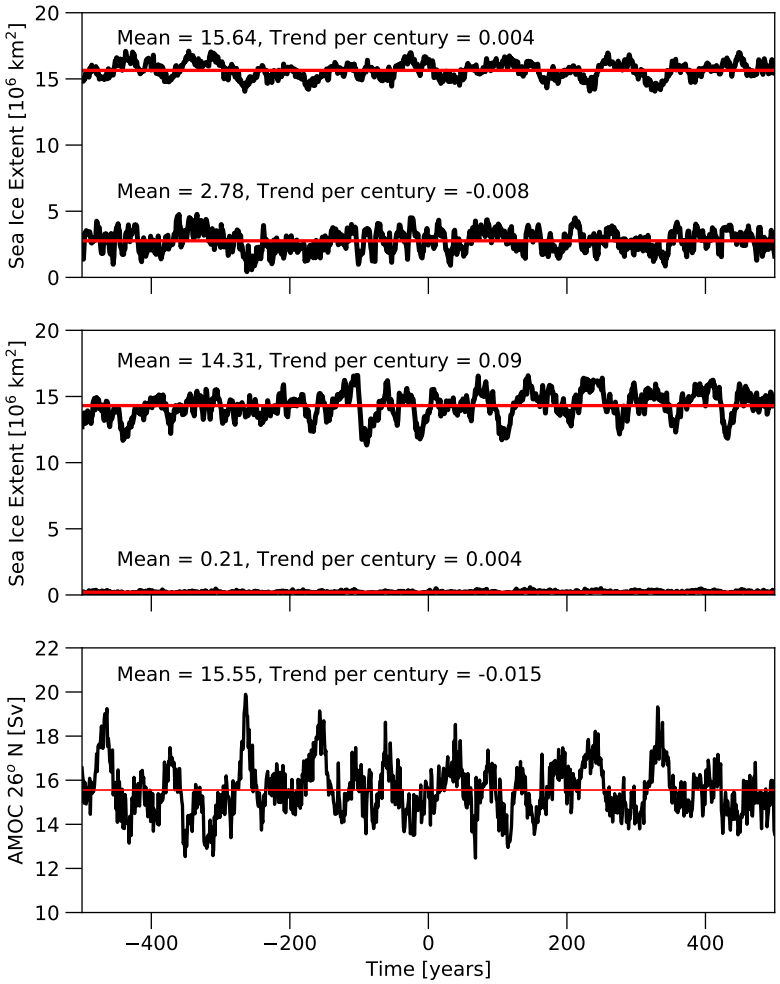

Figure 3. Evolution of key quantities during the last 500 years of the spin-up and the 500-year piControl experiment: maximum and minimum sea-ice extent in million km^2 for a) the Northern Hemisphere and b) the Southern Hemisphere, and c) the strength of the Atlantic Meridional Overturning streamfunction at 26°N and 956m depth in Sverdrup ($1 Sverdrup = 10^6 m^3 s^{-1}$). Red lines indicate the time mean.

4.2 The historical simulation ensemble

4.2.1 Temperature evolution during the historical period

ICON-ESM reproduces the evolution of the global mean surface temperature (GMST) largely in good agreement with observational products (Fig. 4), where anomalies are shown relative to the average over the second half of the 19^{th} century. Note that GMST is used here for comparison with observational products. GMST is a blend of surface air temperature over land and sea surface temperature over the oceans. The mid-20^{th} century warming and the subsequent cooling towards the 1970s agree in magnitude and timing, and the effects of volcanic eruptions like Agung (1963) and Pinatubo (1991) are captured. The simulations slightly disagree with the observational records in the late 20^{th} to early 21^{st} century because the model overestimates the warming trends from the 1970s onward. On the other hand, the warming trends are underestimated near the end of the simulation so that the simulated temperatures agree with the observations at the end

of the simulated period. A decomposition into northern (Fig. 4b) and southern (Fig. 4c) hemispheres reveals that the deviations stem mainly from the northern hemisphere. Assessing the reason for this discrepancy requires further investigations but the more pronounced biases in the northern hemisphere point to an underestimation of the cooling effect of anthropogenic aerosols (Mauritsen et al., 2019) rather than too high climate sensitivity in ICON-ESM (see section 4.4).

4.2.2 Atmosphere

Table 3. Data used for evaluation of atmospheric quantities. Further data used for the computation of skill scores are specified by Crueger et al. (2018).

Quantity	Name	Period	Reference
sea level pressure	ERA-Interim	1979 - 2014	Dee et al. (2011)
zonal mean temperature	ERA-Interim	1979 - 2014	Dee et al. (2011)
zonal mean zonal wind	ERA-Interim	1979 - 2014	Dee et al. (2011)
cloud fraction	CALIPSO-GOCCP (v3.1.2)	2007-2019	Chepfer et al. (2010)
precipitation	GPCP (v2.2)	1979-2013	Adler et al. (2003)
cloud radiative effect	CERES EBAF Ed4.1	2001-2020	Kato et al. (2018)

For the evaluation of atmospheric quantities we follow as closely as possible plotting styles and use of data sets as in Crueger et al. (2018) to enable a comparison of the performance of the coupled ICON-ESM with AMIP-style (i.e. atmosphere-only) simulations by ICON-A and predecessors. Data sets used in the comparison are listed in Table 3. We only use observations and reanalysis data from after the beginning of the satellite era and averages of the 5 members of the historical ensemble for the comparisons.

To allow a quantitative comparison of global model performance with predecessors and uncoupled simulations of this and earlier model versions, we present skill scores for simulated annual mean quantities as proposed by Reichler and Kim (2008) in Fig. 5. Values larger than unity represent larger departures from the observations and are indicative of worse performance relative to the predecessors, and smaller values imply smaller departures from the observations, hence better performance. We calculate these scores in the same way and with respect to the same observational data as described by Crueger et al. (2018). Skill scores for model biases are calculated with respect to model biases in a reference simulation for which we use the historical CMIP6 simulation with the MPI-ESM-LR-1.2 (Mauritsen et al., 2019). It is obvious that the ICON-ESM performs worse than the reference model for many quantities both globally and in the three geographic regions: tropics, northern and southern extratropics. It performs also worse than the predecessor MPI-ESM-LR (Stevens et al., 2013). The performance has clearly improved only for some quantities in the southern extratropics.

In general, a better agreement of uncoupled simulations with observations is expected as they are driven by observed sea surface temperatures and sea ice. This better agreement is clearly visible in Fig. 5, where uncoupled scores for many quantities are below one in most regions, i.e. the agreement with observations is better than in the coupled reference simulation. Differences between our simulation and the uncoupled AMIP experiment of Crueger et al. (2018) are expected due to the coupling, but also due to parameter changes related to the tuning of the coupled model as described in Sections 3.2 and small code modifications as described in Section 2.1. The latter two effects can be estimated from comparing the skill scores of the ICON-ESM AMIP simulation with the

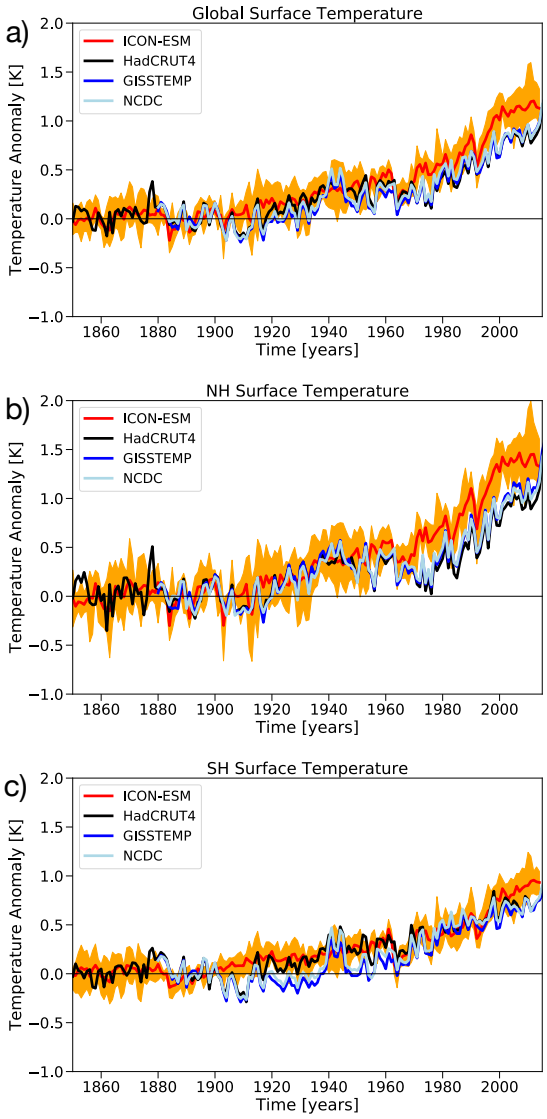

Figure 4. Time series of surface temperature relative to the respective 1850-1899 averages over a) the globe, b) the northern hemisphere, and c) the southern hemisphere for (red-orange) the ICON-ESM historical ensemble, and observational compilations by (blue) the Goddard Institute for Space Studies Surface Temperature product (Lenssen et al., 2019), (black) the blended Hadley Center/Climate Research Unit global temperature data set (Morice et al., 2012), and (light blue) the NOAA NCDC historical merged land–ocean surface temperature data set (Smith et al., 2008; Zhang et al., 2019). The simulated surface temperature is constructed using SSTs over the ocean and surface air temperatures over land.

predecessor ICON-A-1.3.00 used by Crueger et al. (2018). Although some quantities improve, the overall quality in our uncoupled experiment is lower than in the earlier AMIP simulation. A somewhat degraded skill can be expected because our tuning aimed at the performance in the coupled simulation. In the following we evaluate the spatial patterns of some atmospheric quantities.

Figure 6 shows annual mean sea level pressure from the European Center Reanalysis ERA-Interim and the difference of the ICON-ESM to this dataset. Maximum anomalies of up to about 10 hPa are of the same order as anomalies simulated in the uncoupled model (Crueger et al., 2018). However, the spatial structure is very different. While in the uncoupled model there was an underestimation in most parts of the tropics and sub-tropics and a strong positive bias in particular over the Arctic, here we simulate strong positive biases centred near about 45° in both hemispheres. Extratropical biases showed some sensitivity to the SSO parameters (see Table 1) in the tuning process. The positive bias of mean sea-level pressure over the Arctic found in Crueger et al. (2018) could be reduced by activating SSO mountain lift forces of using the parameter *gklift*. The tropical low bias was a feature in all our tuning attempts.

According to the skill scores presented in Fig. 5, the ICON-ESM simulates precipitation over land and ocean in the extratropics similar or even better than predecessors or uncoupled model versions while it still, on average, slightly underestimates precipitation in both southern and northern hemispheric extratropics in comparison to data from the Global Precipitation Climatology Project (GPCP). It performs worse, however, in the tropics. Fig. 7 shows annual mean precipitation patterns in the ICON-ESM in comparison to GPCP data. The model simulates the typical distribution of tropical and extratropical rainfall patterns. In the Pacific, rainfall maxima are too high and a double Intertropical Convergence Zone (ITCZ) bias, typical for many climate models (Tian & Dong, 2020), can be identified. North of the equator the Pacific ITCZ is located too far north, and south of the equator the area of high precipitation extends to far east. These features were also reported for the uncoupled ICON AMIP simulation from Crueger et al. (2018). Improvements with respect to this uncoupled simulation can be identified in the tropical Atlantic and Indian oceans. Concerning the seasonal cycle, a major bias is a shift of maximum precipitation from summer to winter in the boreal forest zone (50N-65N) over the continental interior of Eurasia (not shown), which leads to a large regional deficit in simulated vegetation productivity. In the global mean, the ICON-ESM overestimates precipitation as given by GPCP only by about 3%. With respect to tropical precipitation there is the hope that storm-resolving simulations, i.e. simulations with a horizontal resolution of few kilometers that avoid parameterizing convection, may overcome some of the deficiencies presented here (Fiedler et al., 2020). However, an early intercomparison of such models, including an ICON-A configuration, for a one-month period only, indicated precipitation biases in the Pacific south of the equator that may be reminiscent of the double-ITCZ issue (Stevens et al., 2019).

Figs. 8 and 9 show global annual mean total cloud fraction and zonal mean vertically distributed cloud fraction, respectively, in comparison to the GCM Oriented Cloud Calipso Product (CALIPSO-GOCCP) data. Total cloud fraction is clearly too low in subtropical regions in both hemispheres, a feature which was visible but less strong in the AMIP simulations of Crueger et al. (2018). The vertical distribution of cloud fraction indicates that this is in particular related to an underestimation of low clouds in the subtropics and tropics. High clouds are, by contrast, overestimated in the tropics and middle to high latitudes. Different tuning choices would be able to alleviate these deficiencies, but we did not reach a global energy balance for a realistic global mean temperature and better cloud distributions at the same time.

The global low bias in cloudiness and in particular low level clouds does not necessarily translate directly into a consistent bias of the cloud radiative effect (CRE) as it has been mentioned earlier for other atmospheric models (Nam et al., 2012) and ICON

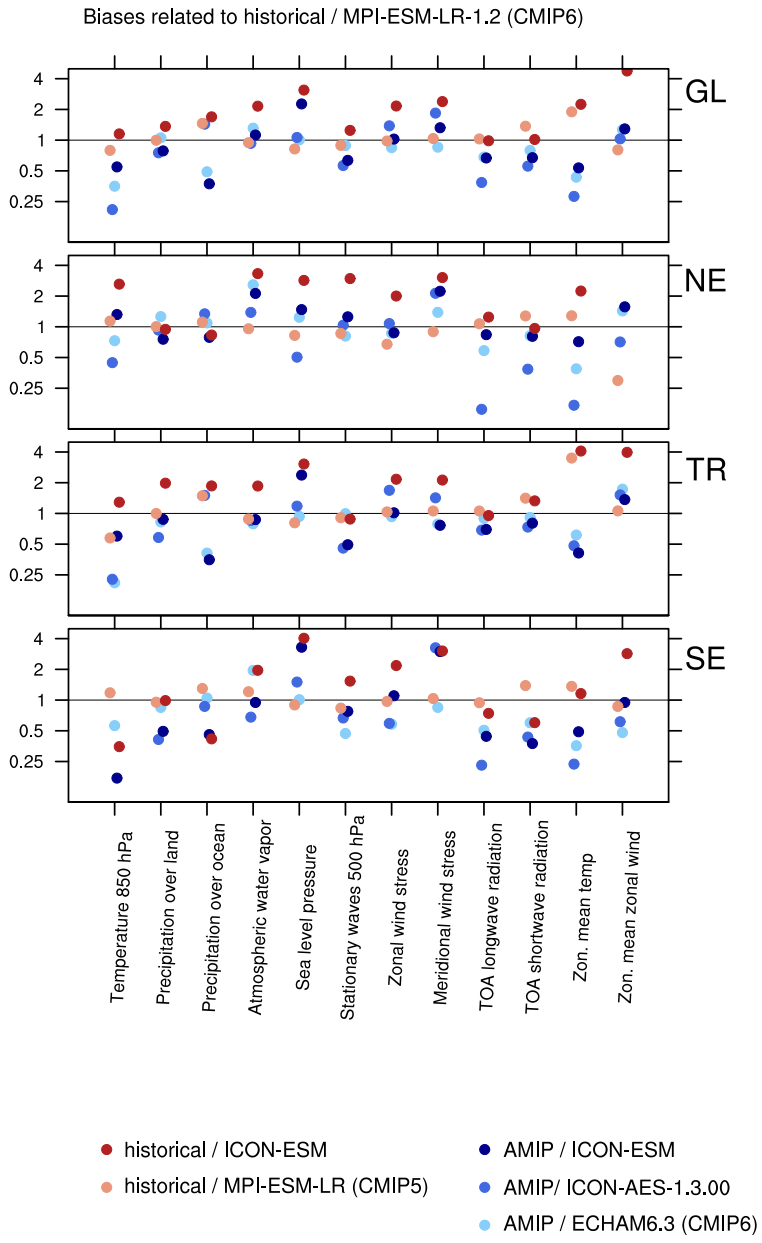

Figure 5. Standardized annual mean climatological errors of selected variables in several simulations with reference to the CMIP6 historical simulation with MPI-ESM-LR-1.2. A value smaller/larger than 1 indicates a smaller/larger bias compared to this reference for the evaluation period 1979 – 2008. Scores are averaged over (from top to bottom) the full globe, the northern extratropics, the tropics (30°S - 30°N), and the southern extratropics. Colored dots indicate scores for the coupled simulations with (red) the ICON-ESM and (orange) the MPI-ESM-LR (Stevens et al., 2013), as well as for the AMIP simulations with (dark blue to light blue) the ICON-ESM, ICON-A-1.3.00 (Crueger et al., 2018), and ECHAM6.3 (Mauritsen et al., 2019). See Section 4.2.2 for further details on the skill scores.

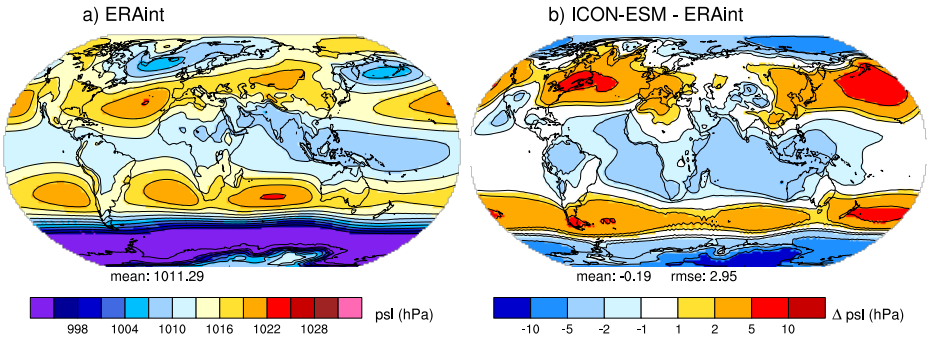

Figure 6. Sea level pressure (hPa) averaged over the period 1979-2014 a) from the ERA-Interim reanalysis and b) difference between ICON-ESM historical simulation and ERA-Interim. Numbers below the panels indicate global means and root mean square difference between simulation and reanalysis.

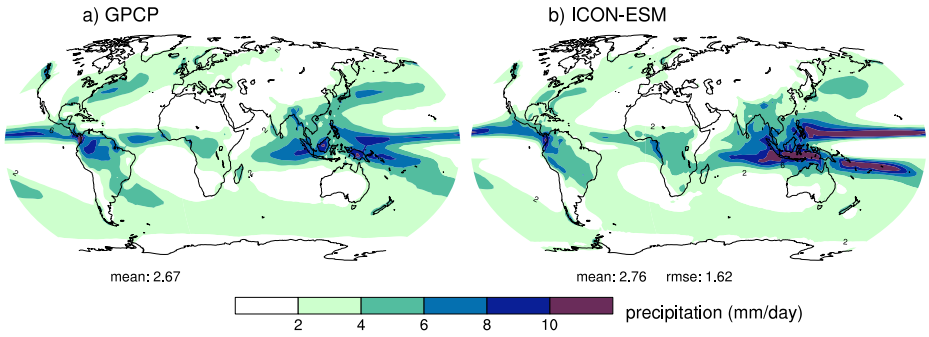

Figure 7. Precipitation (mm/day) a) from the GPCP observations averaged over 1979-2013 and b) from the ICON-ESM historical simulation averaged over 1979-2014 and GPCP. Numbers below the panels indicate global means and root mean square difference between simulation and observation.

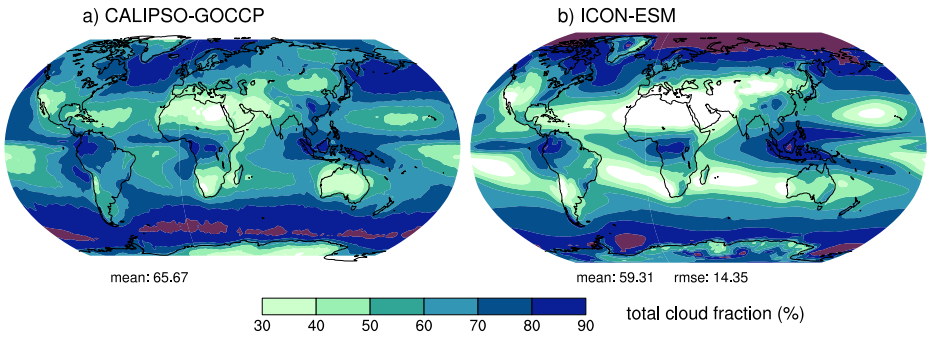

Figure 8. Total cloud fraction (%) a) from the CALIPSO-GOCCP observations averaged over 2007-2019 and b) from the ICON-ESM historical simulation averaged over 1979-2014. Numbers below the panels indicate global means and root mean square difference between simulation and observation.

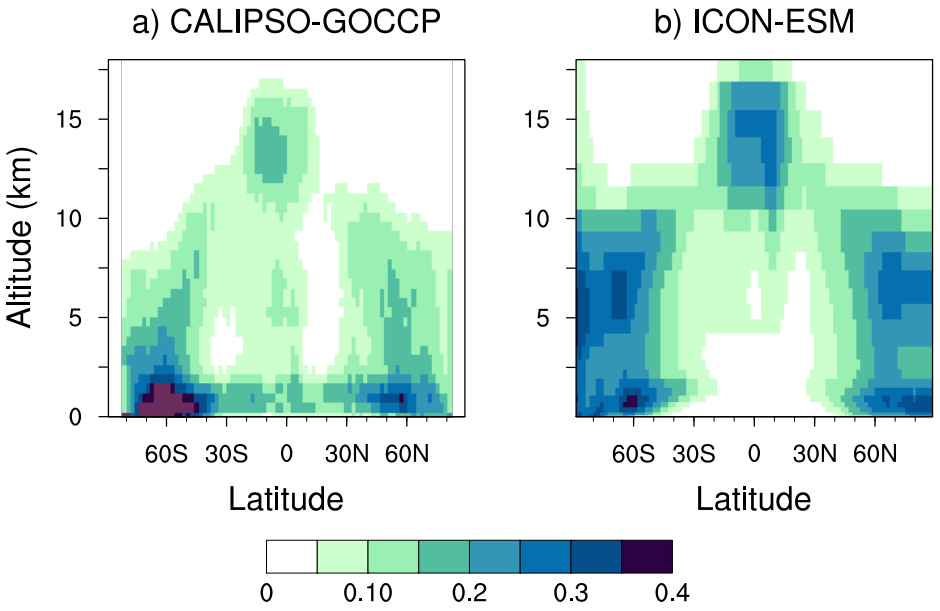

Figure 9. Zonal mean vertical distribution of cloud fraction (%) a) from the CALIPSO-GOCCP observations averaged over 2007-2019 and b) from the ICON-ESM historical simulation averaged over 1979-2014.

predecessors (Crueger et al., 2018). Fig. 10 indicates that the global mean simulated short wave CRE at the TOA is almost equal to the value from the Clouds and Earth's Radiant Energy Systems (CERES) Energy Balanced and Filled (EBAF; we use Edition 4.1) data. The agreement is even better than in the ICON-A AMIP simulations discussed by Crueger et al. (2018) which however had a better net TOA CRE due to almost compensating short and long wave biases. Here, the long wave TOA CRE (not shown) of about 23.5 Wm^{-2} is underestimating the CERES value of about 28 Wm^{-2}. Patterns of both TOA CREs are reproduced fairly realistically as shown for the short wave CRE in Fig. 10. Slight underestimations in the mid-latitudes are compensated by slight overestimations at lower latitudes.

The skill scores indicate that the performance of the ICON-ESM for annual zonal means of both temperature and zonal wind is in general worse than that of its predecessors. In particular, the score for zonal wind is above one, hence indicating stronger departure from the observations, in all geographical regions, but it should be noted, that zonal wind biases were very low for the reference simulation (Fig. B3, Mauritsen et al., 2019). The positive temperature bias in the high latitude middle atmosphere and the cold bias near the high-latitude tropopause (Fig. 11) are recurrent features of our models (Crueger et al., 2018). Their study also discusses that the latter can be reduced by an increase of the vertical model resolution in this region. In the troposphere, the model shows, in general, a warm bias at low and a cold bias at high latitudes. The large zonal wind bias (Fig. 12) is dominated by too strong westerlies in the mid-latitude troposphere and stratosphere, a feature which is strongest in both hemispheres during boreal winter. The position of subtropical jets is biased poleward in both hemispheres. The skill scores of Fig 5 show clearly for both temperature and zonal wind that the ICON-ESM performs worse compared to its atmosphere model in an AMIP simulation. The large increase in biases is, hence, the result of changed atmospheric circulation due to the coupling. Additionally, the current AMIP simulation is performing somewhat worse than

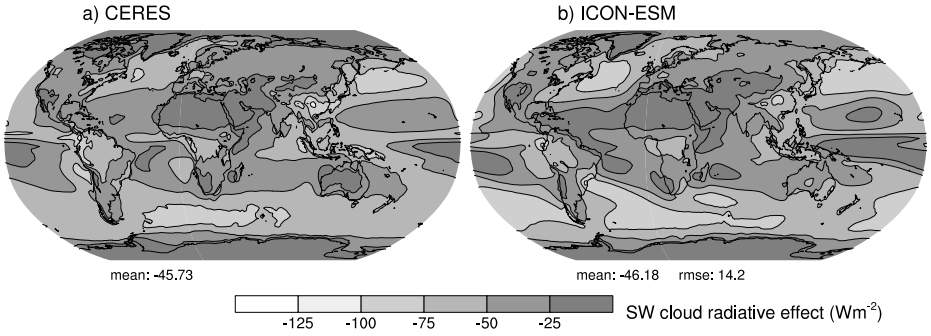

Figure 10. Short wave cloud radiative effect (Wm^{-2}) from a) CERES observations averaged over 2001-2020 and b) from the ICON-ESM historical simulation averaged over 1979-2014. Numbers below the panels indicate global means and root mean square difference between simulation and observation.

the ICON-A configuration (version 1.3.00) from Crueger et al. (2018) which we attribute to the tuning focusing on the coupled model performance. A reduction of the zonal wind biases, and subsequent effects on temperature, would be possible through different tuning choices in the parameterization of SSO effects, but in our tuning experiments this came in general at the expense of larger biases in sea ice and the AMOC.

4.2.3 Land

We compare our model ensemble results for the surface albedo with the Moderate Resolution Imaging Spectroradiometer (MODIS) MCD43C3 CMG Albedo Product (C. Schaaf & Wang, 2015). Cescatti et al. (2012) and C. B. Schaaf et al. (2002) show that the product is suitable for climate model comparisons. It comes with quality information for each data point (quality flags). These flags condense uncertainties in the elicitation of the data, such as atmospheric scattering and absorption, anisotropy, inadequate temporal, spatial and spectral sampling, and narrow-band to broadband conversions. For our comparison we first exclude MODIS data with a low quality of the inversion (quality flags 4 and 5). Then we interpolate the data from the original MODIS grid of 0.05^ox 0.05^o (about 5.6 km at the equator) and from our model grid to a Gaussian lon-lat grid of 96 x 192 (about 1.88^o or 210 km at the equator). As the albedo varies strongly throughout the year due to variations in the angle of the incoming radiation, in leaf area index (LAI), and in snow cover, we take January and July data to represent the boreal winter and summer extremes, for which we average our model results and the MODIS data over the years 2001 till 2014. The differences are shown in Figure 13.

All albedo differences are in the range +/- 0.1. In general the biases are weak as compared to the absolute MODIS albedos. E.g. in January the global near-infrared (NIR) albedo is 0.31 for the absolute values of MODIS, while the corresponding bias is only 0.003. Over glaciers we find a common pattern, where the NIR albedo is too high and the visible (VIS) albedo is too low (see in January over Antarctica and in July over Greenland), which is a direct result of the prescribed minimum and maximum albedo values for glaciers in JSBACH 4. In January, NIR and VIS albedo are too low in the northern mid latitudes, especially in eastern Europe and central Asia. Further analysis reveals that these biases are largely caused by a too small snow cover in JSBACH 4 (not shown). In July, the NIR albedo in eastern North America and large parts of Asia is too low. These low albedos are caused solely by the prescribed soil albedo of the model. Except for the mentioned areas, the albedos tend to be higher in JSBACH 4, e.g. in most of Africa, Australia and

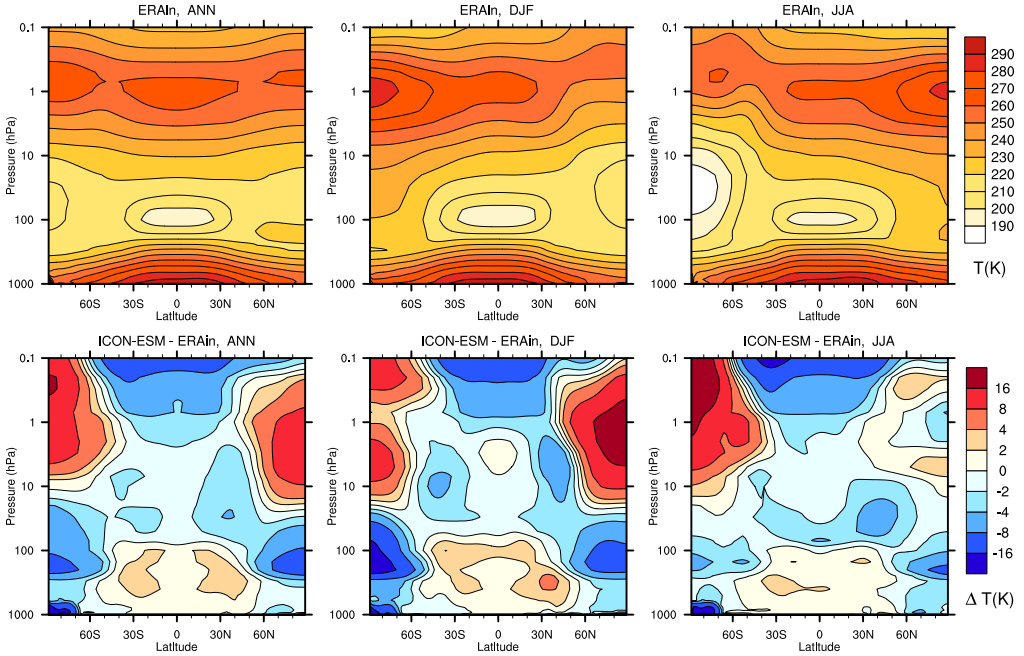

Figure 11. Zonal mean temperature (K) averaged over the period 1979-2014 (top row) from the ERA-Interim reanalysis and (bottom row) difference between ICON-ESM historical simulation and ERA-Interim. From left to right are shown the annual, boreal winter (DJF), and austral winter (JJA) averages.

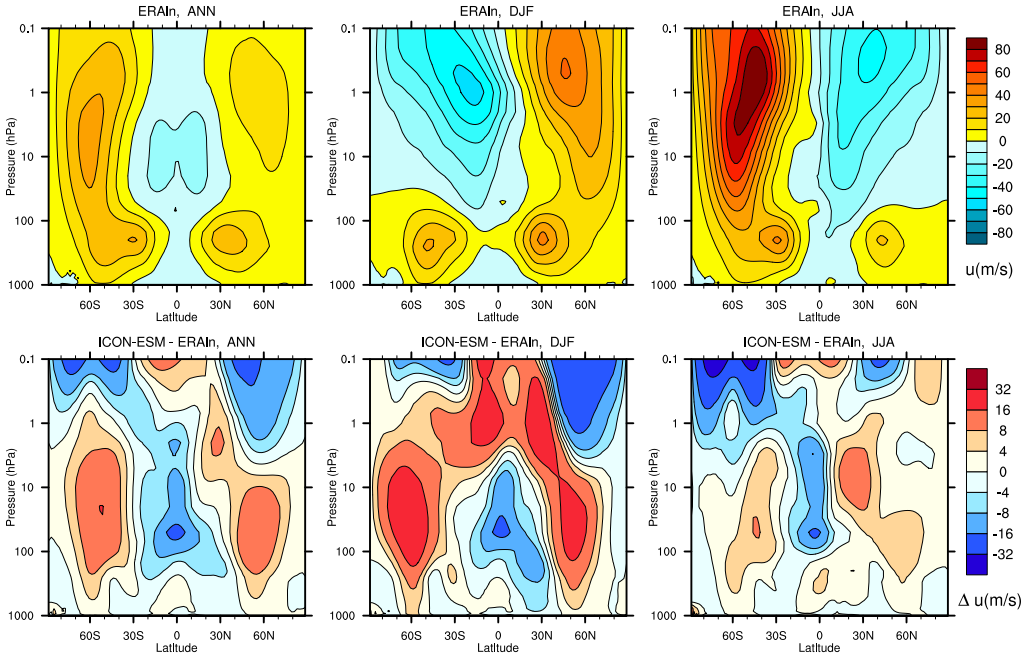

Figure 12. Zonal mean zonal (westerly) wind (ms^{-1}) averaged over the period 1979-2014 (top row) from the ERA-Interim reanalysis and (bottom row) difference between ICON-ESM historical simulation and ERA-Interim. From left to right are shown the annual, boreal winter (DJF), and austral winter (JJA) averages.

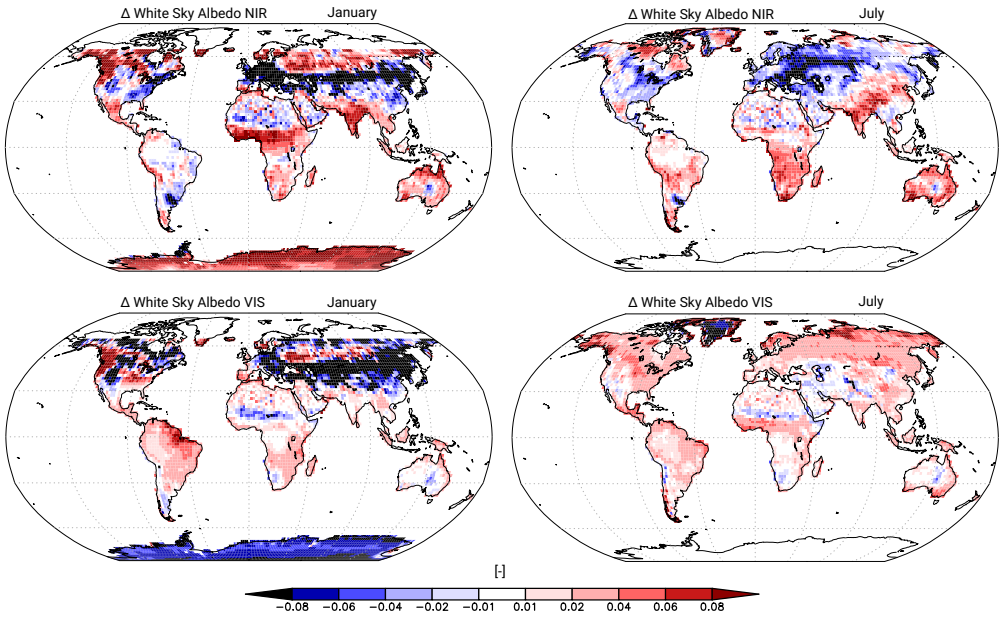

Figure 13. White Sky Albedo (WSA) ICON-ESM historical ensemble minus MODIS data. Shown are the NIR and VIS bands for January and July averaged from 2001 till 2014.

India. However, the causes for this overestimation are rather complex and their investigation is beyond the scope of this paper; a deeper analysis of this issue will be published in a forthcoming paper.

For the evaluation of land surface temperature (LST) of our model ensemble, we use the MOD11C1 MODIS Terra Land Surface Temperature/Emissivity V006 data set (Z. Wan et al., 2015). For our analysis we excluded the data points where the quality flags indicate no retrieval because of clouds. The spatial resolution of the data set is 0.05^o x 0.05^o (about 5.6 km at the equator). Furthermore, we compare our results with the first five ensemble members of the MPI-ESM CMIP6 historical simulations (Wieners et al., 2019).

The global ICON-ESM LST time series (Figure 14, green lines) is highly correlated with the MPI-ESM 1.2 time series (blue lines, correlation coefficient of Spearman 0.93 and of Pearson 0.96) but shows a higher variability in the course of the year (Figure 15). Over the historical period until about 1990, the annual averages of ICON-ESM are slightly colder than those of MPI-ESM 1.2 but are about the same from then on. ICON-ESM is about 0.6^oC warmer than observed by MODIS (red lines) and its variability in the course of the year is nearly the same. Even when on short time scales both models annual means are not in good agreement with the historical Climate Research Unit Temperature (CRUTEM4) reconstruction (Figure 14, black lines), they agree with long term trend (e.g. the temperature rise after 1980).

The geographical LST comparison between ICON-ESM and MODIS averaged between 2001 and 2014 (Figure 16) reveals strong regional differences. The zonal means show a warm bias in the inner tropics and the extratropics. In principle, this can also be seen in the January and July averages. Regionally, the warm bias is throughout the year mostly pronounced in Europe, central Asia, central to north-eastern N-America, the Amazon region, and western Antarctica. The warm bias over Eurasia in January is at least partly caused by the too low snow cover and the associated snow-albedo feedback.

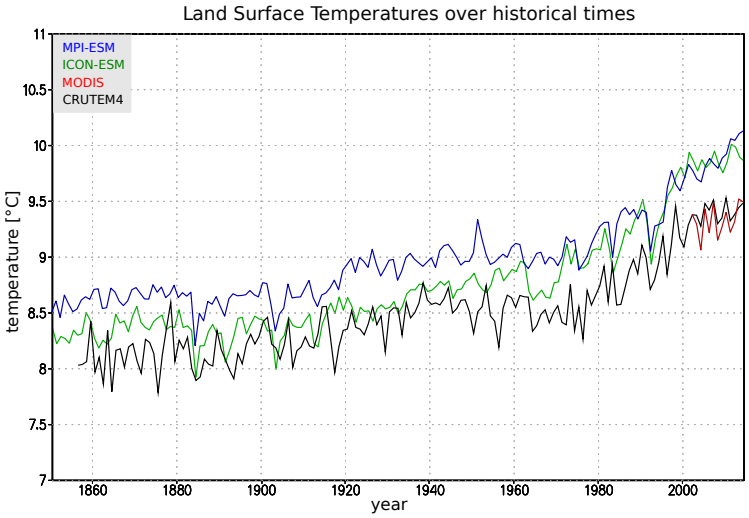

Figure 14. Global Land Surface Temperatures yearly means averaged over historical times. Red: MODIS data. Green: ICON-ESM historical ensemble. Blue: MPI-ESM CMIP6 ensemble mean of the first five ensemble members. Black: CRUTEM4 historical reconstruction. Note, as CRUTEM4 includes only temperature changes without a determined absolute temperature the absolute offset is chosen to fit the curve with the satellite data.

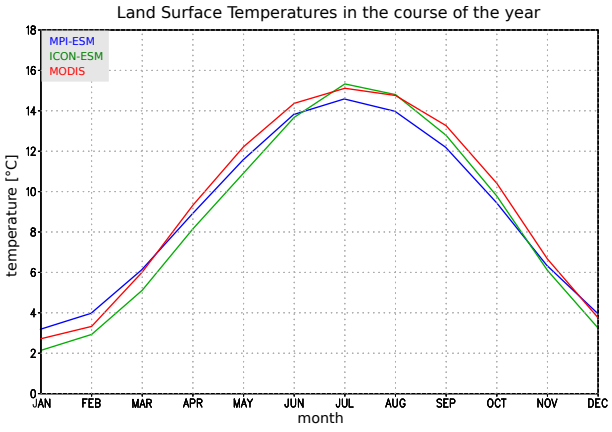

Figure 15. Global Land Surface Temperatures monthly means. Vertical dashed lines indicate the 15th of the respective month. The monthly means are averaged over the available time period of the data plotted in Figure 14.

The comparison with MPI-ESM (Figure 17) shows that the warm bias in Europe, central Asia and Amazonia, which is most pronounced in July, was much weaker or not existent in MPI-ESM. ICON-ESM is colder than the MODIS data in the outer tropics (see zonal means). Regionally, the locations of the cold biases vary with the seasons but Australia, India and central eastern Antarctica (except for the coastal areas) are colder throughout the year. In Australia and central eastern Antarctica the cold bias was much weaker or not existent in MPI-ESM.

Overall, the annual zonal mean bias pattern of ICON-ESM as compared to MODIS is quite symmetric with cool biased subtropics and warm biased extratropics. Due to the complex continental distribution a land origin is implausible. It seems more likely that this pattern is caused by the modeled global atmospheric circulation, i.e. the subtropical cold bias corresponds to the descending air of the Hadley cell. Nevertheless, the albedo biases surely contribute to the LST biases of ICON-ESM, especially in central Asia and over glaciers.

4.2.4 Ocean

The simulated sea surface temperature (SST) obtained from the ensemble mean of the historical simulations and averaged over the period 1980 – 2014 is compared to the PHC 3.0 data set in Figure 18 a, c. Deviations from the observation-based data set are largely smaller than 1^oC over the open oceans, but we diagnose prominent regions with large errors. The most pronounced cold anomalies are found in the subpolar North Atlantic. As in many other coarse-resolution and even eddy-permitting models (e.g., Keeley et al., 2012) this feature is related to an overly zonal North Atlantic Current (Drews et al., 2015) and likely also related to too weak meridional heat transport. For MPI-ESM, Gutjahr et al. (2019) have shown that moving to eddy-resolving resolution in the ocean improves the sub-polar cold bias in the North Atlantic. Corresponding errors in atmospheric sea-level pressure (Fig. 6) indicate that wind-driven circulation biases also contribute to the error. Large atmospheric SLP and circulation biases in the North Pacific are likely responsible for strong warm biases over the Kuroshio region.

The cold-tongue bias in the equatorial Pacific is also a well known model feature, but the ICON-ESM performs less well than the MPI-ESM (Müller et al., 2018), even though MPI-ESM-LR features much lower resolution in the ocean compared to the ICON ocean used here. The bias is a surface expression of the generally too cold sub-surface waters in the tropical oceans (Fig. 19) so that the outcropping isotherms in the central and eastern Pacific are too cold. In the coupled system, the equatorial cold bias is important for the variability characteristics of ENSO and the associated precipitation distribution (section 4.2.7). Warm biases are diagnosed in the upwelling regions at the western coasts of the continents. They are most pronounced at the African coast south of the Equator. These features are common in coupled models and, in particular in the case of Africa, are related to insufficient resolution in the atmosphere where coastal orography and alongshore winds cannot be properly simulated (Milinski et al., 2016).

The sea surface salinity (SSS) biases (Fig. 18b, d) in ICON-ESM are relatively small over most of the oceans, except the high northern latitudes and around the Antarctic continent. The Arctic fresh bias extends also into the sub-polar North Atlantic, where overly fresh water is transported with the gyre circulation into the interior ocean making the cold bias in Fig. 18c a fresh bias as well.

The time-mean biases in zonal averages over the global ocean reflect misrepresentations of water mass pathways and processes like vertical and along-isopycnal mixing. The most prominent error feature in the ICON-ESM ocean is a generally too cold interior ocean with strong cold biases in the sub-tropical and tropical oceans (Fig. 19a) that are accompanied by overly fresh conditions (Fig. 19b). The reasons for the overly strong cooling are not fully understood, but comparison with an earlier version using the

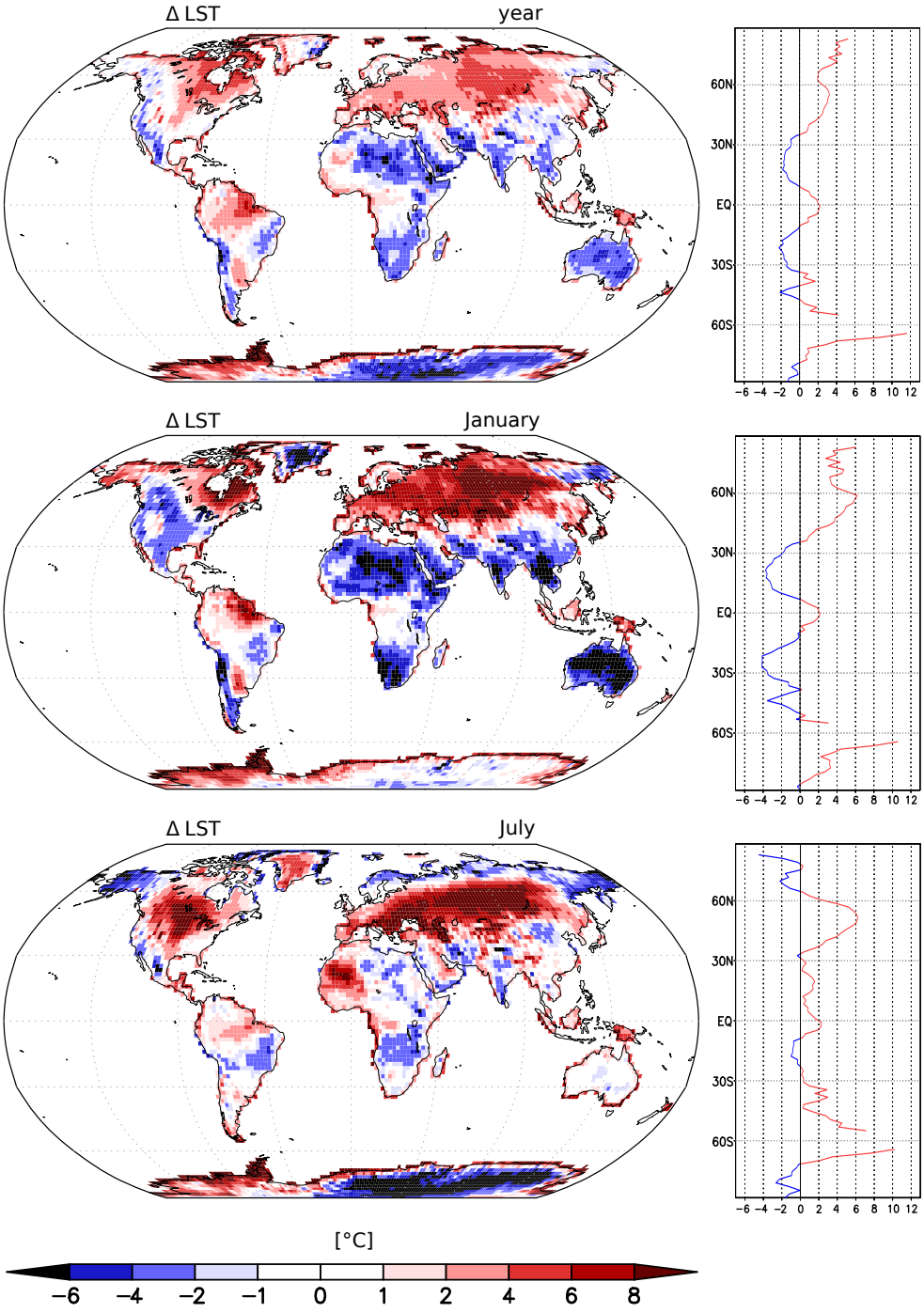

Figure 16. Land surface temperatures in the ICON-ESM historical ensemble minus MODIS data averaged from 2001 to 2014 for all months (top), all January months (middle) and all July months (bottom). The curves on the right side show zonal means.

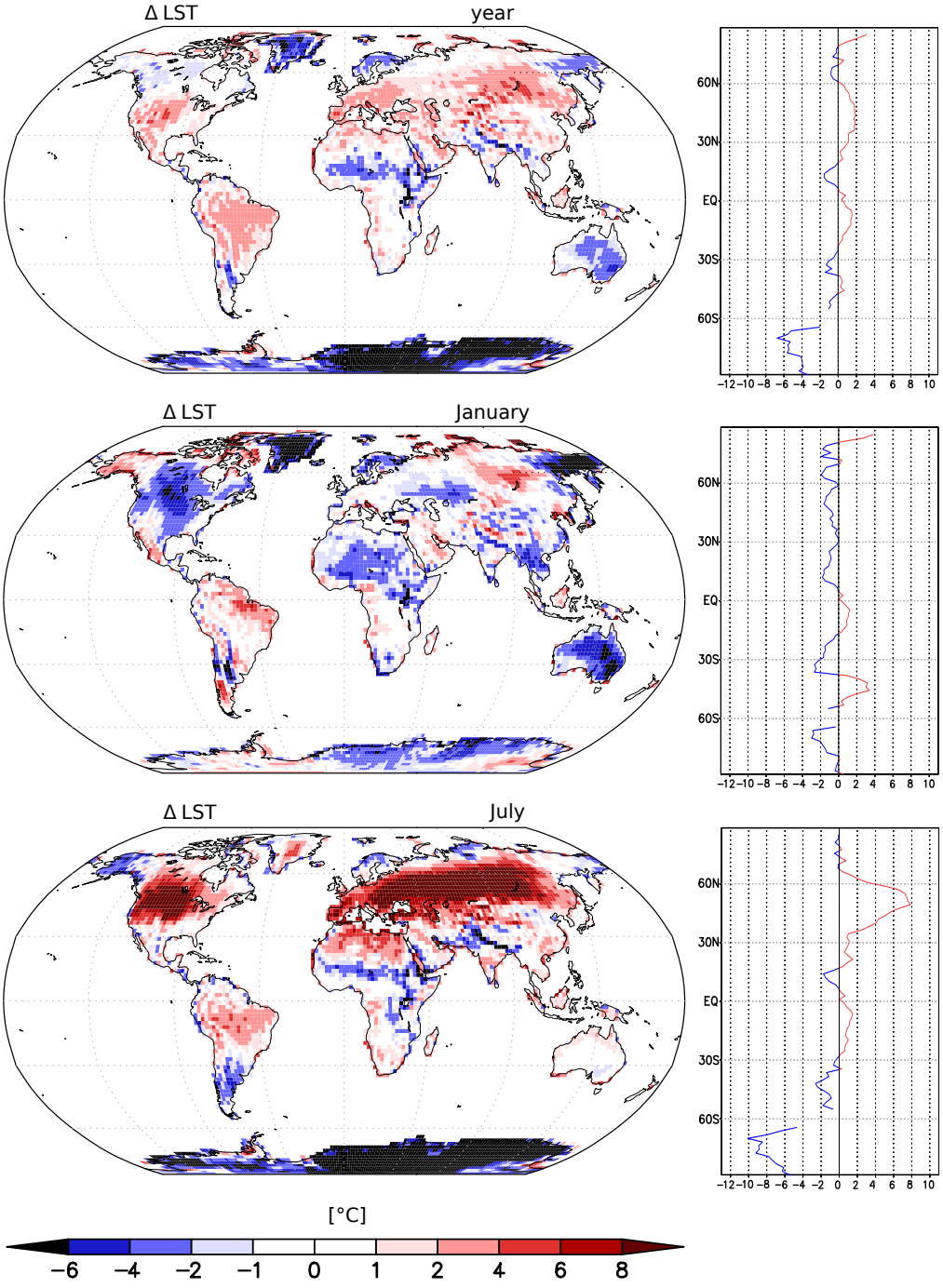

Figure 17. Land surface temperatures in the ICON-ESM historical ensemble minus MPI-ESM ensemble mean averaged from 2001 to 2014 for all months (top), all January months (middle) and all July months (bottom). The curves on the right side show zonal means.

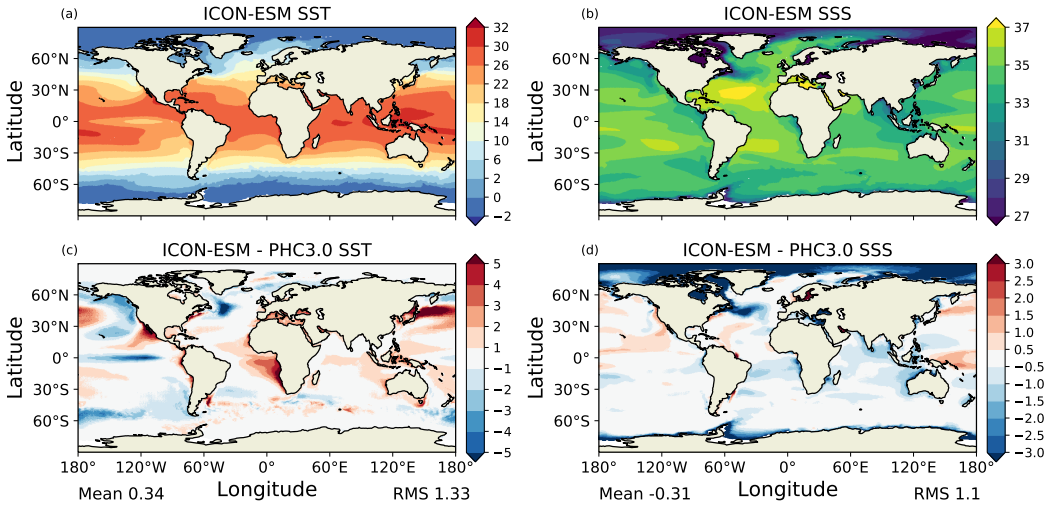

Figure 18. Climatology (1980 -2014) of a) sea surface temperature (SST, in ^{o}C) and b) sea surface salinity (SSS, in PSU) simulated in the ICON-ESM historical simulations together with the model biases for c) SST and d) SSS with respect to the observation-based Polar Science Center Hydrographic Climatology PHC (Steele et al., 2001). The global-mean biases and the root-mean-square (rms) errors are also provided.

Pacanowski-Philander mixing scheme (PP, Pacanowski and Philander (1981)) showed that the PP scheme in combination with the wind-mixing parameterization used in MPIOM (Marsland et al., 2003) showed a better performance than the TKE scheme used here. Regarding the upper ocean, this is consistent with the findings of Gutjahr et al. (2019) for the MPI-ESM. Since the TKE scheme is more advanced and shall be further improved by including an energy-consistent scheme for the background mixing in the interior (see Gutjahr et al., 2021), we decided to keep the TKE scheme and attend to an improved tuning in forthcoming versions of ICON-ESM.

The overly cold sub-thermocline waters lead to a too strong stratification near the thermocline in particular in the tropical oceans and are likely responsible for too strong ENSO variability (see section 4.2.7). The salinity biases resemble those in temperature in the tropical and southern sub-tropical region, but higher northern latitudes feature pronounced positive salinity in the sub-surface ocean. These underlay a too fresh surface layer and lead to a too strong halocline in the Arctic Ocean. The too fresh surface salinities could also be related to an underestimation of Fram Strait fresh water export. While a complete fresh water budget is beyond the scope of this paper, we diagnose a fresh water export through Fram Strait roughly 40% lower than the classical estimate by Aagaard and Carmack (1989).

4.2.5 Large-scale ocean circulation

The AMOC is an important part of the global overturning circulation and it is an important carrier of heat and fresh water in the Atlantic. The AMOC stream function (Fig. 20a) represents the zonally integrated view. Facing west, the North Atlantic Deep Water cell is oriented clockwise and includes the downward motion associated with deep water formation in the Labrador Sea and Nordic Seas, as well as the overflows across the Greenland-Scotland Ridge. The maximum strength of the AMOC exceeds 16 Sv at approximately 40^{o}N and we diagnose an export of about 14 Sv at 30^{o}S. The lower, counter-clockwise oriented cell is associated with Antarctic Bottom Water (AABW) entering the

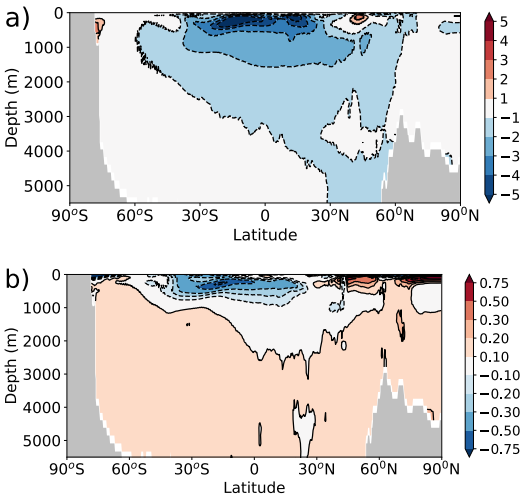

Figure 19. Zonal mean global ocean a) temperature (^{o}C), and b) salinity (PSU) bias relative to the PHC climatology.

Atlantic and upwelling in the basin. The strength of the AABW cell in the North Atlantic is roughly consistent with the observations from the RAPID project, but for the South Atlantic the simulations likely underestimate the AABW inflow. While the simulated AABW maximum is slightly above 2 Sv, observation-based estimates point to values of 6 Sv (Ganachaud & Wunsch, 2003) or 8 Sv (Talley et al., 2003). Although the overturning stream function cannot be compared directly with observation, the RAPID project has provided measurements of the respective flow components at 26.5^{o}N. The profile obtained over more than a decade of observations (Smeed et al., 2018) is shown together with the profiles from the piControl run and the historical simulation (Fig. 20b) and with their variability range estimated from the standard deviation of monthly fields. In the upper ocean, the model reproduces well the shape of the profile, the maximum near 1000 m depth and also the range of variability. The zero crossing is located above 4000 m in the model, but resides roughly 700 meters deeper in the RAPID data. Compared to various versions of MPI-ESM1.2 (Gutjahr et al., 2019) and other CMIP6 models (e.g. Held et al. (2019); Danabasoglu et al. (2020)), which show even shallower NADW cells, the ICON-ESM results are, however, closer to the observations.

Table 4. Simulated and observed net volume transports (Sverdrups) across sections (positive means northward).

Section	ICON-ESM	Obs.	Reference
Bering Strait	0.7-0.8	0.7-1.1	Woodgate et al. (2006, 2012)
Fram Strait	- (2.6-2.8)	-1.75 $\pm$5.01	Fieg et al. (2010)
Denmark Strait	- (4.7-4.9)	-4.8	Hansen et al. (2008)
		-3.4 $\pm$ 1.4	Jochumsen et al. (2012)
Iceland-Scotland	4.7-4.9	4.8	Hansen et al. (2008)
		4.6 $\pm$ 0.25	Rossby and Flagg (2012)
Indonesian Throughflow	9.9-10.1	11.6 - 15.7	Gordon et al. (2010)
Drake Passage	108-112	134.0 $\pm$ 14.0	Nowlin Jr. and Klinck (1986)
		173.3 $\pm$ 10.7	Donohue et al. (2016)

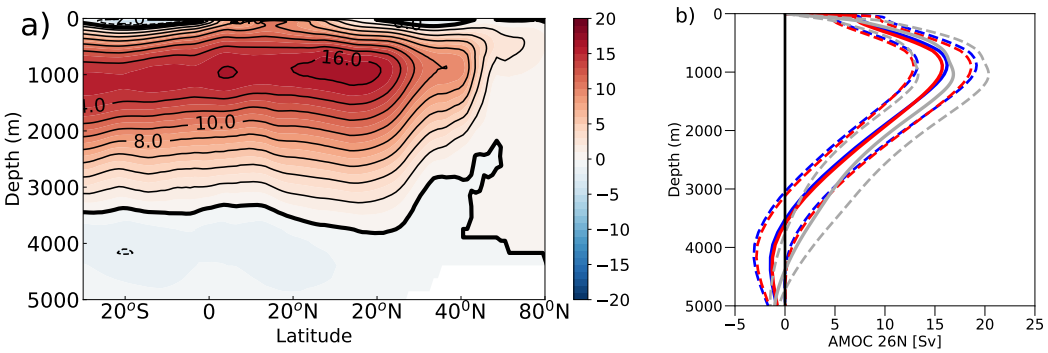

Figure 20. AMOC in ICON-ESM: a) ensemble mean overturning stream function (in Sverdrup, 1 Sv = $10^6 m^3 s^{-1}$) in the Atlantic from the five historical simulations averaged over the period 1980-2014; b) AMOC profile at 26.5N for the historical ensemble (blue) and the piControl simulation (red) together with the observational estimate from RAPID (grey); shown are the mean profiles (thick lines) and the range of variability derived from monthly standard deviations.

The transport through selected passages reflects the representation of the large-scale ocean circulation and can be evaluated in comparison with observational estimates. The total depth-integrated transports through the passages given in Table 4 are mostly simulated within the observational uncertainty found in the literature. The transport through Bering Strait is a key element of the Arctic fresh water budget and the historical simulations are close to the estimates by Woodgate et al. (2006, 2012). The exchange of water masses between the Atlantic Ocean and the Nordic Seas is important for the overturning circulation. The simulated transports are consistent with the circulation scheme by Hansen et al. (2008). The Indonesian Throughflow is another important contributor to the warm-water route of the global conveyor. The simulated transports are slightly underestimated in comparison with the estimate by Gordon et al. (2010). The Drake Passage transport is clearly underestimated in ICON-ESM, both in comparison with the traditional estimate around 135 Sv (Cunningham et al., 2003; Nowlin Jr. & Klinck, 1986) and with the more recent compilation by Donohue et al. (2016). At this stage it is not clear if the mismatch between observed and simulated Drake Passage (and likely Antarctic Circumpolar Current) is related to biases in the wind stresses or the settings of the eddy and background diffusivity in the ocean circulation (P. R. Gent et al., 2001).

The equatorial hydrography and the representation of the zonally-oriented current systems is important for variability features such as Tropical Instability Waves and for coupled ocean-atmosphere phenomena like the El-Nino Southern Oscillation (ENSO). Johnson et al. (2002) provided a compilation of temperature and salinity data and current measurements from the 1990s, which we compare with ICON-ESM results in Figure 21. At 110^{o}W, the placement of the eastward equatorial undercurrent (EUC) and the westward flows on its northern and southern flanks are reproduced well in the model and the depth of the core of the undercurrent lies roughly at the correct depth of 75m (Figure 21a, b). The model underestimates, however, the speeds of the eastward undercurrent and the westward currents flanking the undercurrent. The observed maximum speed of the EUC reads 0.9 ms^{-1} whereas the simulation produces a core speed of about 0.6 ms^{-1}. While the 26^oC isotherm outcrops roughly at the correct position, the near surface waters are up to 4^oC too cold. This results in much stronger stratification and a tighter thermocline. The strong subsurface cold bias is reflected in the pronounced cold bias in the Pacific and the thermocline properties might influence the El Nino Southern Oscillation variability (section 4.2.7). The section along the Equator confirms that

the position of the EUC's core depth is well captured in the model, as are the amplitudes of the EUC and the westward flow near the surface. The weaker EUC seen in Fig. 21 b is therefore more related to a biased longitudinal positioning of the maximum strength of the EUC.

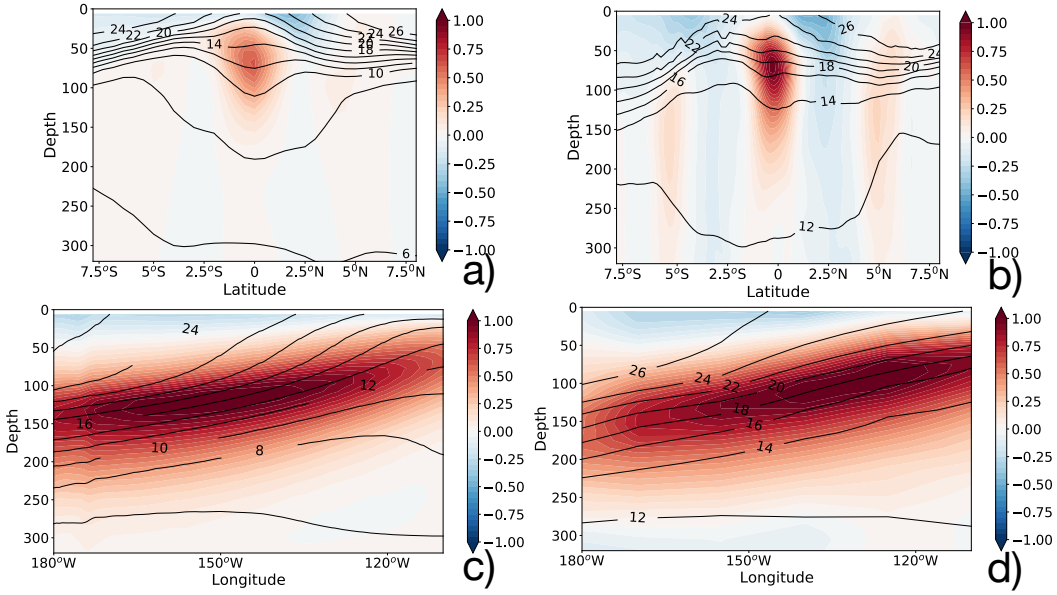

Figure 21. Tropical Pacific zonal velocities (in ms^{-1}, color shading) and temperatures (in ^oC, contour lines) in the ICON-ESM simulation (left) compared to the observation-based estimate by Johnson et al. (2002) (right) at 110^o W (upper row) and along the Equator (lower row).

4.2.6 Sea ice

Sea-ice thickness distributions and extents for late boreal winter and late boreal summer are presented in Figures 22 and 23 for both hemispheres. Arctic and Antarctic sea-ice edges are reproduced in good agreement with the European Organisation for the Exploitation of Meteorological Satellites (EUMETSAT) Satellite Application Facilities on Ocean and Sea Ice (OSI SAF) data set (EUMETSAT, 2015) for the respective winter seasons but summer ice cover is clearly underestimated. Observations indicate that large parts of the Arctic are ice-covered in summer, or at least show sea-ice concentrations above 15%. In contrast the simulated concentrations exceed the 15% threshold only in a relatively small region between Fram Strait and the North Pole. Summer sea ice is also very thin, rarely reaching 1 m thickness. The winter sea-ice thickness distribution is too homogeneous and lacks the typical shape seen in observations (Schweiger et al., 2011) with maximum thicknesses of up to 5m at the northern coast of Greenland and north of the Canadian Archipelago. Deficiencies in the sea-ice thickness distributions are likely related to biases in the atmospheric circulation as indicated by the sea-level pressure errors in Figure 6. Mismatches in the seasonal amplitude and the too thin summer ice need further attention. During the tuning process we tried different options for albedo parameters or the lead-closing scheme. These were either unsuccessful in improving summer sea ice or led to overly large sea-ice extent in winter (in particular in the Labrador Sea) with negative consequences for deep water formation and the strength of the AMOC. Comparing the coupled simulation with a stand-alone ocean run (albeit at somewhat higher horizontal resolution in the Arctic) reveals that the more realistic forcing derived from atmospheric reanalysis leads to a better representation of the sea-

ice distribution, while the forced ocean/sea-ice model also features too thin summer sea ice (c.f., Korn22)

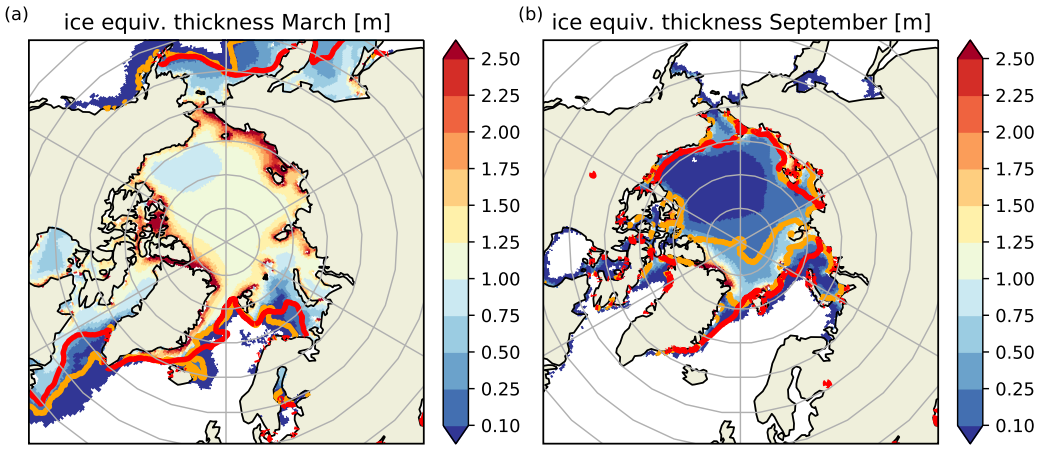

Figure 22. Ensemble mean sea-ice thickness (shading) for a) March and b) September in the northern hemisphere. Thick colored lines depict the 15% sea-ice extent boundary in the simulations (orange) and from the OSI SAF (EUMETSAT, 2015) observational data set (red) averaged over the period 1979 to 2005.

4.2.7 Variability simulated by ICON-ESM

Of the many aspects of climate variability, we have chosen here the El-Nino-Southern Oscillation (ENSO), the Madden-Julian Oscillation (MJO), and the North Atlantic Oscillation (NAO).

ENSO is one of the most important modes of tropical variability with global teleconnections. To analyse characteristic features of ENSO and related quantities we apply the Climate Variability Diagnostics Package (CVDP; Phillips et al., 2014). CVDP allows assessment of simulations in comparison with observation to be carried out in a consistent way. CVDP results presented here can easily be compared with collections of CMIP5 and CMIP6 model evaluations carried out by NCAR (`www.cesm.ucar.edu/workinggroups/CVC/cvdp/data-repository.html`). CVDP provides also links to observational data sets for comparison (the Extended Reconstructed Sea Surface Temperature ERSST (Smith et al., 2008; Huang et al., 2017) and the Hadley Center Sea Surface Temperature HADSST (Rayner et al., 2003) for sea surface temperature and GPCP (Adler et al., 2018) for precipitation). We show here a subset of ENSO features that are based on SST time series from the Nino3.4 region. First, we present spectra (Fig. 24) obtained for boreal winter (DJF) conditions from the five-member historical ensemble (red lines) and from the piControl simulation (blue lines). The latter was split into three sections of 160 years. All time series show a peak near three years and similar variability in the control and historical runs. The spectral peaks are more pronounced than those from the CMIP6 version of the MPI-ESM-LR and the level of variability is considerably higher than the observed spectra. ERSST data as well for the entire period (ERSST5, 1920-2014) as well as those from the last 35 years (ERSST5_1) show a much broader spectrum and indicate less variability on the three-year scale. Regarding the level of spectral power, ICON-ESM is not an exception compared to other CMIP5 and CMIP6 models according to the NCAR repository, but it belongs certainly not to the better performing models. We hypothesize that the sharp spectral peak at three years may be related to the overly strong stratification in the thermocline, which tends to enhance the ther-

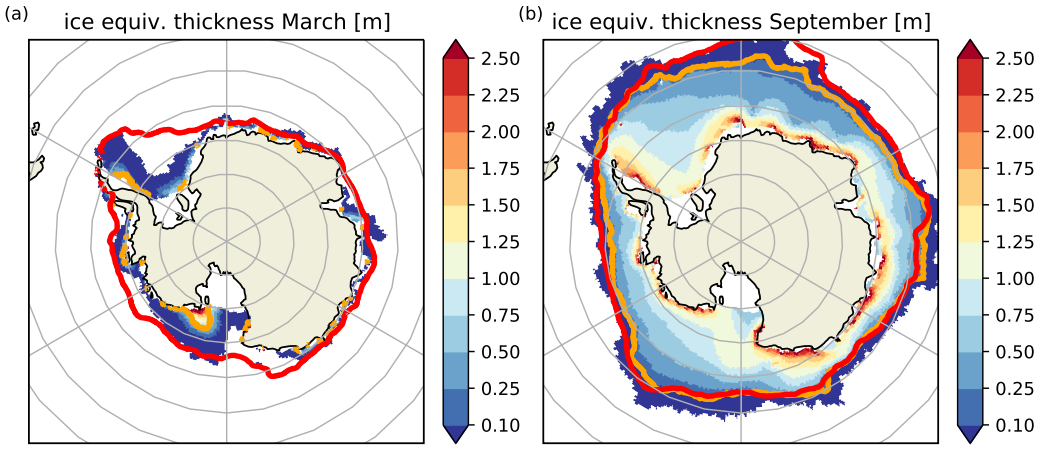

Figure 23. Ensemble mean sea ice thickness (shading) for a) March and b) September in the southern hemisphere. Thick colored lines depict the 15% ice extent boundary in the simulations (orange) and from the OSI SAF (EUMETSAT, 2015) observational data set (red) averaged over the period 1979 to 2005.

mocline feedback (Dewitte et al., 2013). Spatial composites of boreal winter ENSO-related anomalies of temperature and precipitation are shown in Figures 25a and 25b, respectively. While the general patterns are reproduced well, there are deficiencies in reproducing the amplitude of the SST response at the Equator, likely caused by the overly strong thermocline. In particular, positive anomalies reach too far into the warm pool region, where they also shift the positive precipitation anomaly too far to the west (Fig. 25b).

In the tropical atmosphere, convectively coupled equatorial waves show some dependency on the coupling with the SSTs. Therefore, we expect changes with respect to the results of the atmosphere-only version ICON-A (Crueger et al., 2018). Actually, we find an improved signature of the MJO in ICON-ESM, while other waves show weaker power than in ICON-A. This can be assessed by the wave number-frequency spectra of daily precipitation (Kiladis et al., 2009). The GPCP precipitation spectra reveal the strongest power for the waves of the theoretical solutions of the shallow water theory indicated by the solid lines (Wheeler & Kiladis, 1999). In the symmetric spectra, the eastward propagating Kelvin waves for ICON-ESM show less power than the observations and also ICON-A (Fig. 16b, Crueger et al., 2018). On the other hand, the westward propagating Equatorial Rossby waves (ER), often associated with tropical easterly wave disturbances and hurricanes, show a nearly realistic power. A strong improvement is found for the MJO, whose signature is found for wave numbers between 1 to 3 and periods between 30 and 90 days. GPCP and ICON-ESM show a similar power for the MJO. This improvement for ICON-ESM compared to ICON-A confirms that the processes involved in the MJO are actually coupled to the ocean. The antisymmetric ICON-ESM spectrum only shows weak power in the coupled simulation. The eastward propagating inertio-gravity (EIG) or mixed Rossby gravity (MRG) waves are clearly underrepresented compared to GPCP. These results however, are similar to the ICON-A results, indicating that a coupling between atmosphere and ocean does not play a considerable role for these waves.

Another frequently discussed variability pattern is associated with the NAO. Its variations influence the North Atlantic region, water mass conversion in the Labrador Sea, and the European climate. We've calculated the NAO as the leading Empirical Orthogonal Function of sea-level pressure over the area 20^oN to 80^oN and 90^oW to 40^oW

following Hurrell (1995) (not shown). The NAO signature is less pronounced compared to ICON-A (Crueger et al., 2018) and its dipole amplitude clearly underestimated compared to observations. Its positive centre reveals a smaller extent and is displaced northeastward relative to what is observed. In addition, there is no pronounced negative centre. The variance explained by the NAO is smaller in ICON-ESM (43.5%) than in the observations (49.5%). This too weak NAO in ICON-ESM may be related to the too weak extratropical stationary wave pattern (see Fig. 6) in sea level pressure.

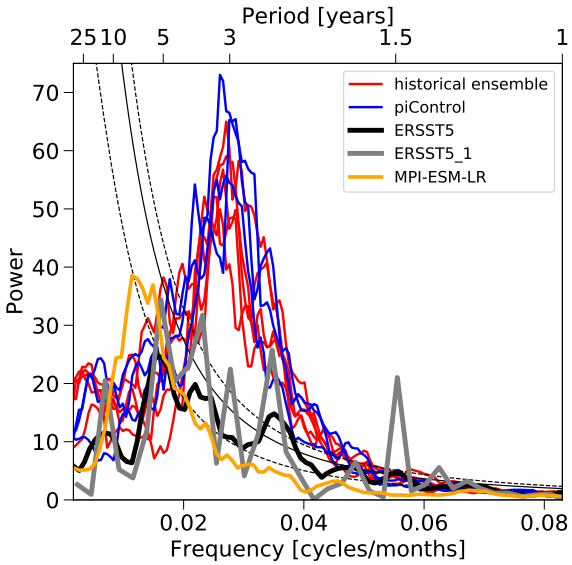

Figure 24. El Nino - Southern Oscillation (ENSO) variability derived from Nino3.4 time series from (red) the historical ensemble, (blue) the piControl simulation, and (orange) a MPI-ESM-LR historical simulation (Mauritsen et al., 2019). The piControl experiment was subdivided into three 160-year long sections. Estimates from the observational ERSST5 data set (Huang et al., 2017) are included, where ERSST5_1 denotes a subset from the last 35 years).

4.3 Ocean biogeochemistry simulated by HAMOCC

The performance of ICON-ESM in simulating the ocean carbon cycle is evaluated in the historical simulation. Only one ensemble member was available including HAMOCC. We compare the climatological mean states of ocean pCO_2, surface phosphate and total alkalinity to observations (Fig. 27). The observational data include pCO_2 compiled by Landschützer et al. (2015) for the time period of 1982-2015 and surface phosphate and total alkalinity from the Global Ocean Data Analysis Project version 2 database (Olsen et al., 2016) for 1972-2014. The modeled data are averaged over the time periods corresponding to their respective observations.

ICON-ESM captures the observed spatial pattern of phosphate concentration. Low concentrations are detected in the subtropical Atlantic and Pacific and Indian Ocean, while the highest concentrations are detected in the North Pacific and Southern Ocean. The surface phosphate is underestimated in the Southern Ocean and eastern equatorial Pacific and overestimated along the southern Chilean coast and in most low-concentration regions such as the subtropical North Atlantic and western Pacific. This pattern of phosphate bias is similar to the simulations of MPI-ESM1.2-HR (Müller et al., 2018).

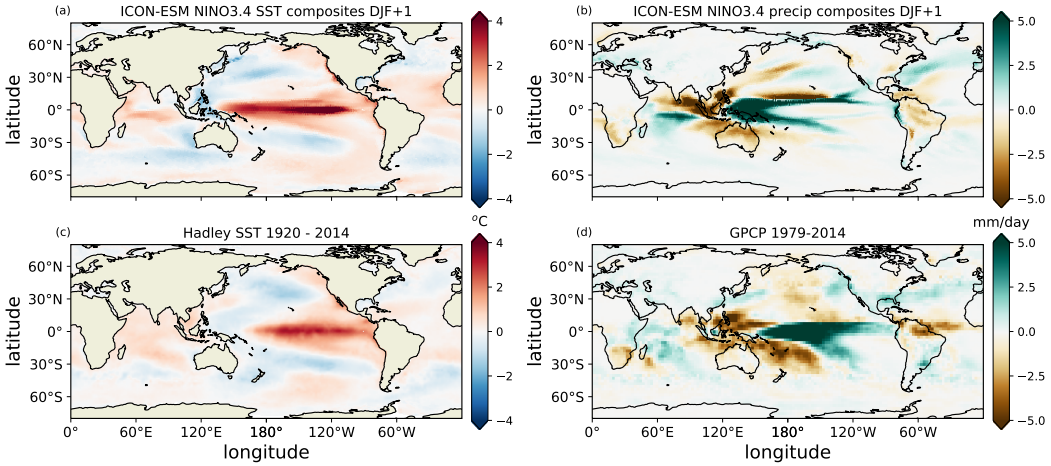

Figure 25. Spatial composites of ENSO (Nino3.4) events for a), c) SST (in ^{o}C), and b), d) precipitation (in mm day^{-1}) from a), b) the historical ensemble mean, c) the HadSST, and d) the GPCP precipitation data sets.

The spatial pattern of the surface total alkalinity also matches the observations, with the highest values in the subtropical Atlantic and Pacific. The bias in surface alkalinity is relatively small in most regions and highly correlated with the SSS bias. A high negative bias in the Arctic extending into the sub-polar North Atlantic is apparent, attributed to the fresh SSS bias.

Regarding the ocean pCO_2, the overall regional pattern is well reproduced, with maximum values detected in the tropical Pacific and minimum values in the extra-tropical regions; but differences are also detected. In the equatorial Pacific, high pCO2 biases are detected, with negative biases in the eastern equatorial Pacific and positive bias in the western equatorial Pacific. In general, ICON-ESM simulates higher pCO_2 over most of the oceans compared to observations. This is mainly attributed to positive SST biases in most regions or negative alkalinity biases in the areas with fresh SSS bias. In addition, ICON-ESM simulates a lower net global ocean carbon sink compared to observations (not shown). ICON-ESM simulates a decadal mean net ocean carbon sink of 1.61 GtC/yr for 2000-2009, which is on the lowest range of 2.1±0.5 GtC/yr reported by the Global Carbon Budget (Friedlingstein et al., 2020).

4.4 Idealized CO_2 increase simulations and climate sensitivity

Two measures of the model's response to changes in radiative forcing are computed using the idealized CO_2-increase experiments in CMIP6 DECK: Transient Climate Response (TCR) and Equilibrium Climate Sensitivity (ECS). TCR is computed from the experiment where CO_2 increases by 1 percent per year (1pctCO2). The TCR is estimated as the GSAT increase around the time of CO_2-doubling, which happens after 70 years of simulation. To minimize effects of internal variability we take a 20-year average between years 60 and 79 as suggested by Meehl et al. (2020) and we arrive at a TCR of 2.1K. This value is slightly higher than the 1.8 K derived for the CMIP6 version of MPI-ESM-LR and in the middle of the range found in the CMIP6 multi-model assessment by Meehl et al. (2020). Differences in TCR are often related to variations in the ocean heat content changes under global warming, which could be different in MPIOM and ICON-O due to different formulations of vertical mixing and the GM parameters (Semmler et al., 2021). ECS is estimated using the DECK "abrupt4xCO2" experiment applying the

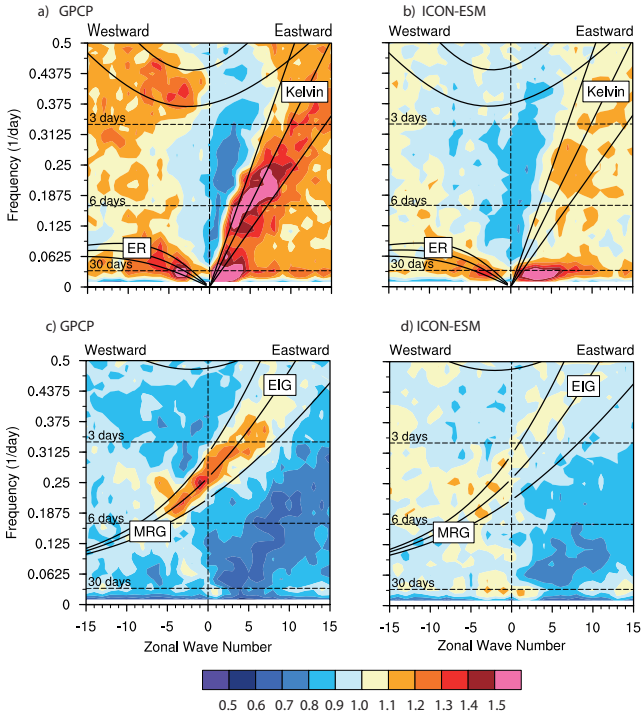

Figure 26. Wave number-frequency power spectra of the symmetric (upper) and antisymmetric (lower) component of precipitation, summed from 13°N to 13°S, plotted as ratios between raw power and the power of smoothed red noise background spectra from GPCP (a, c) and ICON-ESM V1.0 (b, d) and Positive/negative wave numbers represent eastward/westward propagating waves. Horizontal dashed lines represent periods of 3, 6, and 30 days. Solid lines represent the solutions of the shallow-water equations: for the symmetric components Kelvin and equatorial Rossby (ER) waves and for the anti-symmetric components inertio gravity waves (EIG) and mixed Rossby gravity (MRG) waves. In (a) and (b) the Madden-Julian Oscillation (MJO) signal appears with strong power on the eastward propagating part with wave numbers 1–3 and periods longer than 30 days (Kiladis et al., 2009). Analysis period is 1997–2014, as in Crueger et al. (2018).

method of Gregory et al. (2004), which has also been used by Meehl et al. (2020). We perform a linear regression between the GSAT and the net downward radiative flux at the top-of-atmosphere over 150 years of simulation. ECS is then estimated from an extrapolation of the regression line to zero net heat imbalance (Fig. 28b). This procedure results in an ECS of 3.7 K, which can be compared with the value of 2.9 in MPI-ESM-LR. MPI-ESM and ICON-ESM are quite similar in their estimate of the effective forcing (estimated as the crossing of the regression lines with the y-axis in Fig. 28b), but the slopes of the regression lines are considerably different. We note that the change of temperature over time differs for the later part of the experiments. Redoing the ECS estimation excluding the first 20 years in the regression, we find a much higher value of 4.3 K in ICON, whereas there is only a relatively small change to 3.1 K in MPI-ESM. This difference is likely related to different evolution of local or regional feedbacks (Armour et al., 2013). However, for the ICON-ESM no effort was made to tune the climate sensitivity in order to better match the historical record as it was done for MPI-ESM1.2 (Mauritsen & Roeckner, 2020). ICON-ESM's ECS values are higher than those of its predecessors,

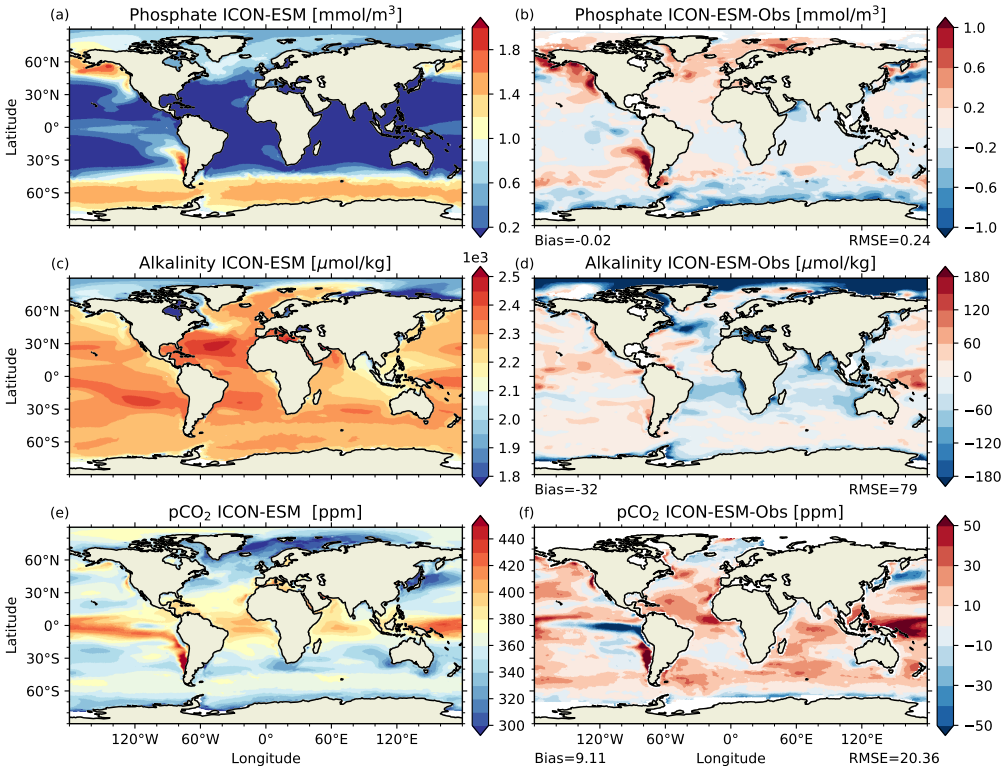

Figure 27. Climatological mean state of ocean biogeochemical variables from ICON-ESM (left column) and ICON-ESM minus observation (right column). The shown variables are ocean surface pCO_2 (top row), surface phosphate concentration (middle row), and total alkalinity (bottom row). The observed pCO_2 data are from Landschützer et al. (2015) and phosphate and total alkalinity data are from the Global Ocean Data Analysis Project version 2 database

but are considerably lower than the estimates from several new CMIP6 models (Meehl et al., 2020) (often exceeding 5 K). ICON-ESM's ECS lies well in the 5-95% range of 2.3 to 4.7 K estimated from "multiple lines of evidence" by Sherwood et al. (2020).

5 Discussion

During the tuning phase we have explored different parameter settings and, in the case of ocean vertical mixing, the choice between two different parameterization schemes (TKE, PP, see section 2.2). We started the coupled experiments using parameter settings inherited from the stand-alone ocean and atmosphere simulations. While these gave good or at least acceptable results in ICON-A (Crueger et al., 2018) and ICON-O (Korn22), solutions meeting our tuning goals (see Section 3) were much harder to obtain.

Problematic biases increased or became more apparent as feedbacks between the coupled components evolved. For example, the ICON-A AMIP simulation described in Crueger et al. (2018) exhibits relatively good skill scores, but features strong positive sea-level pressure biases in high northern latitudes (their Figure 3). In the coupled simulation, this error is accompanied by too weak winds over the subpolar North Atlantic that could lead to biases in ocean circulation, water mass transformation and, eventually, to a strong reduction or collapse of the AMOC. Changing parameter settings in the SSO

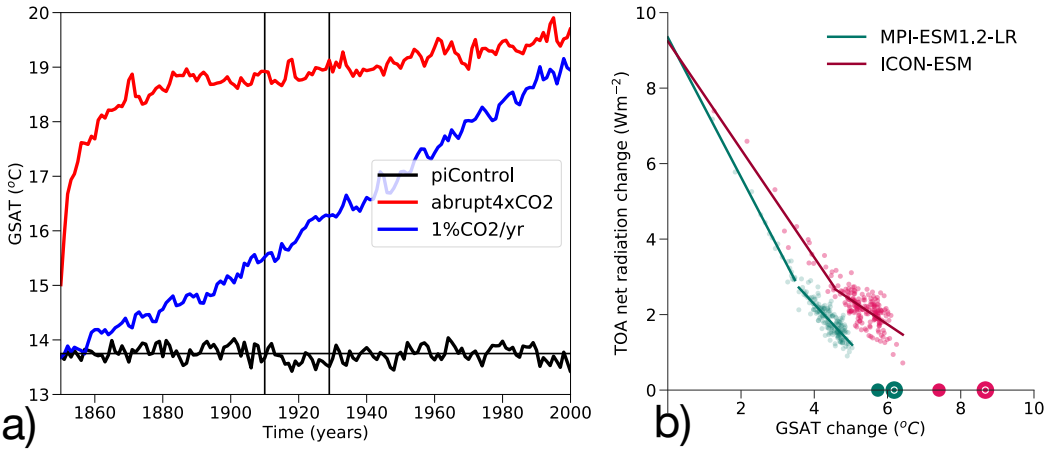

Figure 28. Estimating the Transient Climate Response (TCR) and Equilibrium Climate Sensitivity (ECS) from idealized DECK experiments. a) Evolution of global surface air temperature in the $1pctCO2$ (blue) and $abrupt4XCO2$ (red) together with the $piControl$ experiment (black). Vertical lines indicate the period for the TCR calculation, b) regression analyses to estimate ECS in ICON-ESM (dark red) and in MPI-ESM1.2. The small dots on the horizontal axis indicate twice the ECS based on a regression using the first 150 years following Gregory et al. (2004). The bigger dots show the respective intersection of the regression based on years 20 to 200.

parameterization (see Table 1) turned out to be an effective way to reduce the SLP bias. However, for instance, small values of *gkdrag* reducing SLP biases also led to stronger errors in upper tropospheric and stratospheric zonal wind strength and distribution. Therefore, the results presented here are the results of compromises. Avoiding detrimental effects in some key quantities, such as the collapse of the AMOC or a freeze-over of the Labrador Sea in the ocean, required sometimes parameter settings in the atmosphere that turned out to be sub-optimal in terms of atmospheric performance skill scores (Figure 5).

In general, we found that tuning choices had often complex and unexpected effects in the coupled system. Partly, these were hard to grasp as they require relatively long adjustment times. Experience gained in uncoupled simulations can often not be transferred to the coupled system, and feedbacks working in the coupled system may modify or overrule the effects. Moreover, obtaining a tuning target is often dependent on several parameter settings and these may influence each other. We demonstrate this with the example of the AMOC strength taken from several ICON-ESM experiments (at least 100-year long) with different parameter settings. ICON-O stand-alone experiments, where only the coefficients for isoneutral diffusion K and the thickness diffusion according to the GM parameterization κ have been changed, indicated that larger K and κ lead to weaker overall AMOC strength, likely due to a stronger flattening of isopycnals. This behavior has been analyzed by Marshall et al. (2017) in stand-alone ocean model configurations. However, an inspection of the multitude of coupled experiments leads us to conclude that it is possible to arrive at any AMOC state even for K and κ set to zero. We found fewer solutions with weak overturning at high K and κ, but this may be due to the smaller number of experiments. It is also difficult to relate the AMOC strength uniquely to other parameters. For example, the experiments run with K/κ equal 400 ms^{-2} in Figure 29 come with various settings of the wave drag parameter *gkdrag* and an inspection of this column in isolation would lead us to conclude that lower wave drag parameters produce higher ocean overturning, possibly due to the effects on wind stress,

and subsequently ocean and sea-ice circulation. As has been demonstrated by Putrasahan et al. (2019) and K. Lohmann et al. (2021) for MPI-ESM, wind stress changes influence sea-ice exports from the Arctic and cross-basin exchanges of salinity in the sub-polar North Atlantic resulting in modifications of deep-water formation and AMOC strength. But again, looking at all experiments using a moderately low *gkdrag* of 0.02 we find an AMOC range between 7.6 and almost 25 Sv. We conclude that a more thorough multi-cause/multi-parameter investigation on the sensitivity of the AMOC is required for the coupled ICON-ESM.

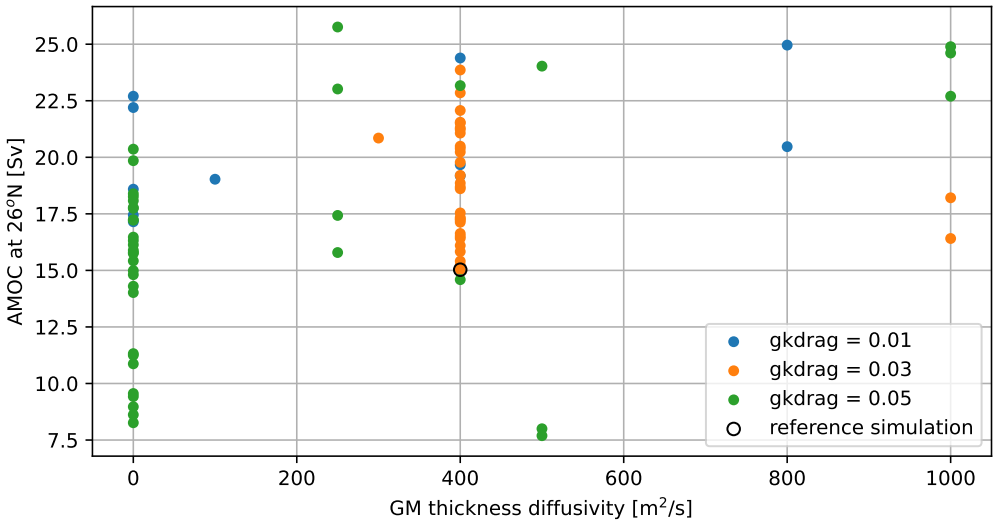

Figure 29. Scatterplot relating the thickness diffusion parameter according to the GM parameterization κ with the strength of the AMOC at 26°N. The black circle indicates the standard experiment (piControl) and colors refer to different choices of the gravity wave drag parameter *gkdrag*. Shown are experiments with a runtime of at least 100 years.

It is obvious that another round of tuning and an even more extensive set of sensitivity experiments could have improved some of the shortcomings mentioned above. We decided, however, to finalize "version 1" at this stage to set a milestone in the model development. Moreover, model development activities in the component models have continued in parallel and we prefer to postpone a second round of major tuning efforts until some innovations can be included in the standard model configurations. We mention here two developments in ICON-O: the z* vertical coordinate and a newly developed dynamical sea-ice model. z* is designated to replace "z-level" as standard coordinate and comes together with an improved representation of the bottom topography in the form of "partial cells", which was already implemented in MPIOM and its predecessors. The implementation process includes a slight reorganization of level distribution in the upper ocean and we plan to achieve a better representation of the mixed layer processes and mixing by re-assessing the TKE parameterization. Mehlmann and Korn (2021) have developed a novel sea-ice dynamics formulation, which is based on an analogue of the Arakawa-CD grid. The CD-grid placement has appealing resolving properties at high spatial resolution compared to traditionally used discretizations (Mehlmann et al., 2021). Furthermore, the development allows a straightforward coupling to the Arakawa C-grid-like discretization used in ICON-O. As the new sea ice dynamics are realized on the same grid as ICON-O the coupling does not require rotations (c.f. section 2.3) and promises a better representation of the bathymetry. While the deficits in the simulated sea-ice cli-

matology documented here may be related to problems in sea-ice thermodynamics, we expect improvement from the new dynamics, e.g., for the representation of narrow passages and the related ice transports. By affecting fresh-water exchanges, the latter could lead to improvements in water mass properties and air-sea exchanges for example in the Labrador Sea.

Ongoing development work will further explore ICON-specific opportunities like grid refinement in ICON-O (Logemann et al., 2021) and nesting in the atmosphere (Jungandreas et al., 2021). The excellent scaling capabilities of ICON have been documented in the DYAMOND project with ICON-A setups between 80 and 2.5 km (Stevens et al., 2019; Hohenegger et al., 2020) and are further explored in very high resolution coupled setups with grid spacing of a few kilometers in the DYAMOND-WINTER project (`https://www.esiwace.eu/services/dyamond/winter`).

While the ICON-A version described herein uses the physical parameterization package inherited from ECHAM6 (Stevens et al., 2013; Giorgetta et al., 2018), which was designed for "climate" applications at grid sizes from 50 to 350 km, higher-resolution ICON application will require other choices. At km-scale, some parameterizations may become obsolete or will be better represented by schemes from the numerical weather-prediction version of ICON (Zängl et al., 2015). Therefore, a longer-term goal of the ICON community is the development of a system for "seamless" predictions from weather to climate scales.

6 Summary and conclusions

In this paper, we have documented ICON-ESM (V1.0), the first coupled model that is based on the ICON framework (Zängl et al., 2015) with its icosahedral grid concept. We have presented the first simulations with the coupled ICON-ESM confronting it with the task to deliver reasonable results in a well-defined experimental framework, the CMIP6 DECK simulations, and we have published the results on the Earth System Grid Federation (ESGF) repository (Lorenz et al., 2021). Coupling of the newly developed component models and the tuning of the coupled model turned out to be more challenging than expected. Tuning choices that revealed robust results in stand-alone simulations needed adjustment or reconfiguration in the presence of coupled feedbacks. The performance of the ICON-ESM reported in this paper can be summarized as follows:

1. We were able to fulfil the primary tuning goals: The 500-year long piControl simulation exhibits little drift in key quantities like GSAT, radiation, sea-ice cover, and the AMOC. TOA radiation is well balanced with little remaining drift. GSAT and other global quantities are close to observational estimates for the pre-industrial climate.

2. A set of five historical simulations reproduces the observed global surface temperature evolution largely in agreement with observational data sets, albeit with somewhat too strong warming in the second half of the 20th century.

3. ICON-ESM's climate sensitivities (TCR, ECS) are slightly higher than the corresponding values from MPI-ESM, but well in the range of the CMIP6 multi-model ensemble (Meehl et al., 2020), and the recent estimate based on multiple lines of evidence by Sherwood et al. (2020).

4. The present-day climate simulated for the last decades reproduces largely the climatology from observations and reanalyses, but biases are often larger than in ICON-ESM's predecessor model MPI-ESM1.2 and other CMIP6 models.

5. The tuning of the ocean carbon cycle component represented by the model HAMOCC has been performed resulting in a stable piControl state with adequately represented dis-

tributions of the key ocean biogeochemical variables, like phosphate, total alkalinity and pCO_2.

6. Ocean carbon cycle in the historical simulation is overall in good agreement with observations regarding regional patterns and absolute values. Mismatches between modeled and observed patterns are to a first order attributable to the biases in SST and SSS. Overall, this shows a high sensitivity of ocean biogeochemical parameters to the underlying physical state of the ocean.

Problematic issues identified in the analyses are: In the atmosphere, the representation of both low-level and high-level clouds showed considerable deficiencies. Bias patterns, which were already identified in stand-alone atmosphere simulations became more pronounced in the coupled system. Counter-tuning that could have improved cloud distributions had negative side effects on other parts of the climate system. Skill scores based on wind and temperature data are worse than in MPI-ESM. In particular zonal wind biases remain and there is some indication that the parameterization of sub-grid scale orographic effects requires further attention.

Overall, the rather zonal pattern of the land surface temperature biases hints to the global atmospheric circulation as their major cause. Nevertheless, the winter land surface temperatures show regional biases that may be traced to a misrepresentation of surface albedo values. The biases over Antarctica and Greenland partly reflect albedo deviations over glaciers. Errors in land temperatures over Eurasia are substantially caused by a too low snow cover and the associated snow-albedo feedback. The biases could be partly improved by changes in the near-infrared and visible albedo settings in JSBACH 4, but others are complex and related to deficits in snow cover or soil and canopy albedo biases.

In the ocean, SST and SSS climatologies show bias patterns and magnitudes comparable to other coarse-resolution CMIP5 or CMIP6 models, whereas the relatively large sub-surface biases are of concern in particular in the tropical oceans. Here, a re-tuning of the vertical mixing scheme might alleviate misrepresentation of wind-induced mixing. From improvements in the upper-ocean stratification we expect also positive effects on ENSO variability and processes in the tropical oceans. Northern hemisphere sea ice concentrations is somewhat too high in winter with too much ice cover, for example in the Labrador Sea. On the other hand, the seasonal cycle is too strong leading to too thin sea-ice in summer with only half of the Arctic basis being ice-covered in summer. The seasonal cycle is also too strong in the southern hemisphere.

ENSO variability in ICON-ESM is less close to observations than MPI-ESM's, but similar to many other CMIP5 and CMIP6 models. The spectra derived from Nino3.4 time-series of the historical simulations show a too narrow peak at about three years and an overly high level of variance. The spatial patterns associated to ENSO variability agree with the observed ones, but there are too strong signals in the warm pool and in the Indian Ocean.

We emphasize that the present configuration is the first milestone in establishing ICON-ESM as a highly flexible modelling system. ICON-ESM V1 serves as a basis for further developments that will take advantage of ICON-specific properties such as spatially varying resolution, and coupled configurations at resolutions of a few kilometers in atmosphere, land, and ocean.

7 Data Availability Statement

The data from the ICON-ESM V1.0 DECK simulations are available at the CMIP6 repository of the Earth System Grid Federation (Lorenz et al., 2021) and can be accessed at `http://esgf-data.dkrz.de/search/cmip6-dkrz/`. The model code of ICON is avail-

able to individuals under licenses (`https://mpimet.mpg.de/en/science/modeling-with-icon/code-availability`). By downloading the ICON source code, the user accepts the licence agreement. The source code of the ICON-ESM-V1.0 used in this study, primary data, and scripts used in the analyses and for producing the figures can be obtained from the WDCC Long Term Archive (`http://cera-www.dkrz.de/WDCC/ui/Compact.jsp?acronym=RUBY-0_ICON-_ESM_V1.0_Model`).

Acknowledgments

We thank the German Climate Computer Centre DKRZ for providing the computational resources. TI was supported by the European Union's Horizon 2020 research and innovation program under grant agreement No 101003536 (ESM2025 – Earth System Models for the Future) and under grant agreement No 820989 (COMFORT)". TI and FC were supported by the Deutsche Forschungsgemeinschaft (DFG, German Research Foundation) under Germany's Excellence Strategy - EXC 2037 'Climate Climatic Change and Society' (CLICCS) - Project Number: 390683824 and by the European Union's Horizon 2020 research and innovation programme under grant agreement number 773421 - project "Nunataryuk"." This paper is a contribution to the project S2 (PIs JJ and NB) of the Collaborative Research Centre TRR 181 "Energy Transfers in Atmosphere and Ocean" funded by the Deutsche Forschungsgemeinschaft (DFG, German Research Foundation) - Project nr. 274762653. HP received funding by DWD's "Innovation Programme for Applied Researches and Developments" (IAFE VH3.5). FZ was supported by the German Federal Ministry of Education and Research (BMBF) as a Research for Sustainability initiative (FONA) through the project PalMod (FKZ: 01LP1502A) and by the European Union's Horizon 2020 research and innovation programme under grant agreement No 823988 (ESiWACE2). The CMIP6 participation received funding by the BMBF via the project CMIP6-DICAD (FKZ: 01LP1605A). We thank David Salas y Melia and three anonymous reviewers for constructive comments that helped improving the manuscript.

References

Aagaard, K., & Carmack, E. C. (1989). The role of sea ice and other fresh water in the arctic circulation. *Journal of Geophysical Research: Oceans*, *94*(C10), 14485–14498.

Adcroft, A., & Campin, J.-M. (2004). Rescaled height coordinates for accurate representation of free-surface flows in ocean circulation models. *Ocean Modelling*, *7*(3-4), 269–284.

Adler, R. F., Huffman, G. J., Chang, A., Ferraro, R., Xie, P.-P., Janowiak, J., ... others (2003). The version-2 global precipitation climatology project (gpcp) monthly precipitation analysis (1979–present). *Journal of Hydrometeorology*, *4*(6), 1147–1167.

Adler, R. F., Sapiano, M. R., Huffman, G. J., Wang, J.-J., Gu, G., Bolvin, D., ... others (2018). The global precipitation climatology project (gpcp) monthly analysis (new version 2.3) and a review of 2017 global precipitation. *Atmosphere*, *9*(4), 138.

Armour, K. C., Bitz, C. M., & Roe, G. H. (2013). Time-varying climate sensitivity from regional feedbacks. *Journal of Climate*, *26*(13), 4518–4534.

Axell, L. B. (2002). Wind-driven internal waves and Langmuir circulations in a numerical ocean model of the southern Baltic Sea. *J. Geophys. Res.*, *107(C11)*, 3204. doi: 10.1029/2001JC000922.

Becker, J., Sandwell, D., Smith, W., Braud, J., Binder, B., Depner, J., ... others (2009). Global bathymetry and elevation data at 30 arc seconds resolution: Srtm30_plus. *Marine Geodesy*, *32*(4), 355–371.

Bopp, L., Resplandy, L., Orr, J. C., Doney, S. C., Dunne, J. P., Gehlen, M., ... others (2013). Multiple stressors of ocean ecosystems in the 21st century:

projections with cmip5 models. *Biogeosciences*, *10*(10), 6225–6245.

Borchert, S., Zhou, G., Baldauf, M., Schmidt, H., Zängl, G., & Reinert, D. (2019). The upper-atmosphere extension of the icon general circulation model (version: ua-icon-1.0). *Geoscientific Model Development*, *12*(8), 3541–3569.

Brovkin, V., Raddatz, T., Reick, C. H., Claussen, M., & Gayler, V. (2009). Global biogeophysical interactions between forest and climate. *Geophysical research letters*, *36*(7). doi: 10.1029/2009GL037543

Cescatti, A., Marcolla, B., Vannan, S. K. S., Pan, J. Y., Román, M. O., Yang, X., ... others (2012). Intercomparison of MODIS albedo retrievals and in situ measurements across the global FLUXNET network. *Remote sensing of environment*, *121*, 323–334.

Chen, C., Liu, H., & Beardsley, R. C. (2003). An unstructured grid, finite-volume, three-dimensional, primitive equations ocean model: Application to coastal ocean and estuaries. *Journal of Atmospheric and Oceanic Technology*, *20*(1), 159–186. doi: 10.1175/1520-0426(2003)020⟨0159:augfvt⟩2.0.co;2

Chepfer, H., Bony, S., Winker, D., Cesana, G., Dufresne, J., Minnis, P., ... Zeng, S. (2010). The gcm-oriented calipso cloud product (calipso-goccp). *Journal of Geophysical Research: Atmospheres*, *115*(D4).

Crueger, T., Giorgetta, M. A., Brokopf, R., Esch, M., Fiedler, S., Hohenegger, C., ... Stevens, B. (2018). ICON-A, The Atmosphere Component of the ICON Earth System Model: II. Model Evaluation [Journal Article]. *Journal of Advances in Modeling Earth Systems*, *10*(7), 1638-1662. doi: 10.1029/2017ms001233

Cunningham, S. A., Alderson, S. G., King, B. A., & Brandon, M. A. (2003). Transport and variability of the Antarctic circumpolar current in Drake Passage. *J. Geophys. Res., 108 (C5)*, 8084. doi: 10.1029/2001JC001147

Danabasoglu, G., Lamarque, J.-F., Bacmeister, J., Bailey, D., DuVivier, A., Edwards, J., ... others (2020). The Community Earth System Model version 2 (CESM2). *Journal of Advances in Modeling Earth Systems*, *12*(2).

Danilov, S. (2013). Ocean modeling on unstructured meshes. *Ocean Modelling*, *69*, 195–210. doi: 10.1016/j.ocemod.2013.05.005

Danilov, S., Wang, Q., Timmermann, R., Iakovlev, N., Sidorenko, D., Kimmritz, M., ... Schröter, J. (2016). Finite-Element Sea Ice Model (FESIM), version 2. *Geoscientific Model Development Discussions*, *8*, 1747–1761.

Dee, D. P., Uppala, S. M., Simmons, A., Berrisford, P., Poli, P., Kobayashi, S., ... others (2011). The era-interim reanalysis: Configuration and performance of the data assimilation system. *Quarterly Journal of the Royal Meteorological Society*, *137*(656), 553–597.

de Vrese, P., Stacke, T., Kleinen, T., & Brovkin, V. (2021). Diverging responses of high-latitude co 2 and ch 4 emissions in idealized climate change scenarios. *The Cryosphere*, *15*(2), 1097–1130. doi: 10.5194/tc-15-1097-2021

Dewitte, B., Yeh, S.-W., & Thual, S. (2013, 08). Reinterpreting the thermocline feedback in the central-western pacific and its relationship with the enso modulation. *Climate Dynamics*, *41*, 819–830. doi: 10.1007/s00382-012-1504-z

Donohue, K. A., Tracey, K. L., Watts, D. R., Chidichimo, M. P., & Chereskin, T. K. (2016). Mean Antarctic Circumpolar Current transport measured in Drake Passage. *Geophys. Res. Lett.*, *43*, 11760–11767. doi: 10.1002/2016GL070319

Drews, A., Greatbatch, R. J., Ding, H., Latif, M., & Park, W. (2015). The use of a flow field correction technique for alleviating the North Atlantic cold bias with application to the Kiel Climate Model [Journal Article]. *Ocean Dynamics*, *65*(8), 1079-1093. doi: 10.1007/s10236-015-0853-7

Ekici, A., Beer, C., Hagemann, S., Boike, J., Langer, M., & Hauck, C. (2014, apr). Simulating high-latitude permafrost regions by the JSBACH terrestrial ecosystem model. *Geoscientific Model Development*, *7*(2), 631–647. doi: 10.5194/gmd-7-631-2014

EUMETSAT, O. (2015). *Global sea ice concentration reprocessing dataset 1978–2015 (v1. 2).*

Eyring, V., Bony, S., Meehl, G. A., Senior, C. A., Stevens, B., Stouffer, R. J., & Taylor, K. E. (2016). Overview of the Coupled Model Intercomparison Project Phase 6 (CMIP6) experimental design and organization [Journal Article]. *Geoscientific Model Development*, *9*(5), 1937-1958. doi: 10.5194/gmd-9-1937-2016

Fiedler, S., Crueger, T., D'Agostino, R., Peters, K., Becker, T., Leutwyler, D., ... others (2020). Simulated tropical precipitation assessed across three major phases of the coupled model intercomparison project (cmip). *Monthly Weather Review*, *148*(9), 3653–3680.

Fieg, K., Gerdes, R., Fahrbach, E., Beszczynska-Möller, A., & Schauer, U. (2010). Simulation of oceanic volume transports through Fram Strait 1995–2005. *Ocean Dyn.*, *60*, 491–502. doi: 10.1007/s10236-010-0263-9

Friedlingstein, P., O'sullivan, M., Jones, M. W., Andrew, R. M., Hauck, J., Olsen, A., ... others (2020). Global carbon budget 2020. *Earth System Science Data*, *12*(4), 3269–3340.

Ganachaud, A., & Wunsch, C. (2003). Large-scale ocean heat and freshwater transports during the World Ocean Circulation Experiment [Journal Article]. *Journal of Climate*, *16*(4), 696-705. doi: Doi10.1175/1520-0442(2003)016⟨0696:Lsohaf⟩2.0.Co;2

Gaspar, P., Grégoris, Y., & Levefre, J.-M. (1990). A Simple Eddy Kinetic Energy Model for Simulations of the Oceanic Vertical Mixing Tests at Station Papa and Long-Term Upper Ocean Study Site. *Journal of Geophysical Research: Oceans*, *95*(C9), 16179-16193.

Gent, P., & McWilliams, J. (1990). Isopycnal mixing in ocean circulation models. *Journal of Physical Oceanography*, *20*, 150–155.

Gent, P. R., Large, W. G., & Bryan, F. O. (2001). What sets the mean transport through Drake Passage? *Journal of Geophysical Research: Oceans*, *106*(C2), 2693–2712.

Giorgetta, M. A., Brokopf, R., Crueger, T., Esch, M., Fiedler, S., Helmert, J., ... Stevens, B. (2018). ICON-A, the Atmosphere Component of the ICON Earth System Model: I. Model Description. *Journal of Advances in Modeling Earth Systems*, *10*(7), 1613-1637. doi: 10.1029/2017ms001242

Giorgetta, M. A., Jungclaus, J., Reick, C. H., Legutke, S., Bader, J., Bottinger, M., ... Stevens, B. (2013). Climate and carbon cycle changes from 1850 to 2100 in MPI-ESM simulations for the Coupled Model Intercomparison Project phase 5. *Journal of Advances in Modeling Earth Systems*, *5*(3), 572–597. doi: 10.1002/jame.20038

GLCC. (2018). *Glcc global land cover characterization.* (Tech. Rep.). United States Geological Survey Land Cover Products. doi: doi:10.5066/F7GB230D

Golaz, J. C., Caldwell, P. M., Van Roekel, L. P., Petersen, M. R., Tang, Q., Wolfe, J. D., ... Zhu, Q. (2019). The DOE E3SM Coupled Model Version 1: Overview and Evaluation at Standard Resolution. *Journal of Advances in Modeling Earth Systems*, *11*(7), 2089–2129. doi: 10.1029/2018ms001603

Goll, D. S., Winkler, A. J., Raddatz, T., Dong, N., Prentice, I. C., Ciais, P., & Brovkin, V. (2017). Carbon–nitrogen interactions in idealized simulations with jsbach (version 3.10). *Geoscientific Model Development*, *10*(5), 2009–2030. doi: 10.5194/gmd-10-2009-2017

Gordon, A. L., Sprinthall, J., Van Aken, H. M., Susanto, D., Wijffels, S., Molcard, R., ... Wirasantosa, S. (2010). The Indonesian throughflow during 2004–2006 as observed by the INSTANT program. *Dyn. Atmos. Oceans*, *50*, 115–128. doi: 10.1016/j.dynatmoce.2009.12.002

Gregory, J. M., Ingram, W. J., Palmer, M. A., Jones, G. S., Stott, P. A., Thorpe, R. B., ... Williams, K. D. (2004). A new method for diagnosing radiative

forcing and climate sensitivity. *Geophysical research letters*, *31*(3), L03205. doi: 10.1029/2003GL018747

Griffies, S. (1998). The gent-mcwilliams skew flux. *Journal of Physical Oceanography*, *28*, 831–841.

Griffies, S., Gnanadesikan, A., Pacanowski, R. C., Larichev, V., Dukowicz, J., & Smith, R. (1998). Isoneutral diffusion in a z-coordinate model. *Journal of Physical Oceanography*, *28*, 831–841.

Griffies, S. M., Levy, M., Adcroft, A. J., Danabasoglu, R., Hallberg, R. W., Jacobsen, D., ... Ringler, T. D. (2015). *Theory and numerics of the Community Ocean Vertical Mixing (CVMix) Project* (Tech. Rep.). Princeton, NJ: NOAA/Geophysical Fluid Dynamics Laboratory. Retrieved from `https://github.com/CVMix/CVMix-description`

Gutjahr, O., Brüggemann, N., Haak, H., Jungclaus, J. H., Putrasahan, D. A., Lohmann, K., & von Storch, J.-S. (2021). Comparison of ocean vertical mixing schemes in the Max Plank Institute Earth System Model (MPI-ESM1.2). *Geoscientific Model Development*, *14*, 2317—2349. doi: 10.5194/gmd-14-2317-2021

Gutjahr, O., Putrasahan, D., Lohmann, K., Jungclaus, J. H., von Storch, J. S., Brüggemann, N., ... Stössel, A. (2019). Max Planck Institute Earth System Model (MPI-ESM1.2) for the High-Resolution Model Intercomparison Project (HighResMIP). *Geoscientific Model Development*, *12*(7), 3241–3281. doi: 10.5194/gmd-12-3241-2019

Hagemann, S., & Dümenil, L. (1997). A parametrization of the lateral waterflow for the global scale. *Climate Dynamics*, *14*, 17–31. doi: 10.1007/s003820050205

Hanke, M., & Redler, R. (2019). *New features with yac 1.5.0.* (Vol. 3; Tech. Rep.). doi: 10.5676/DWD_pub/nwv/icon_003

Hanke, M., Redler, R., Holfeld, T., & Yastremsky, M. (2016). YAC 1.2.0: new aspects for coupling software in Earth system modelling. *Geoscientific Model Development*, *9*(8), 2755–2769. doi: 10.5194/gmd-9-2755-2016

Hansen, B., Østerhus, S., Turrell, W. R., Jónsson, S., Valdimarsson, H., Hátún, H., & Olsen, S. M. (2008). The Inflow of Atlantic Water, Heat, and Salt to the Nordic Seas Across the Greenland–Scotland Ridge. In R. R. Dickson, J. Meincke, & P. Rhines (Eds.), *Arctic–Subarctic Ocean Fluxes: Defining the Role of the Northern Seas in Climate* (pp. 15–43). Dordrecht: Springer Netherlands. doi: 10.1007/978-1-4020-6774-7_2

Hawkins, E., & Sutton, R. (2016). Connecting Climate Model Projections of Global Temperature Change with the Real World. *Bulletin of the American Meteorological Society*, *97*(6), 963–980. doi: 10.1175/Bams-D-14-00154.1

Held, I. M., Guo, H., Adcroft, A., Dunne, J. P., Horowitz, L. W., Krasting, J., ... Zadeh, N. (2019). Structure and Performance of GFDL's CM4.0 Climate Model. *Journal of Advances in Modeling Earth Systems*, *11*(11), 3691–3727. doi: 10.1029/2019ms001829

Hines, C. O. (1997). Doppler-spread parameterization of gravity wave momentum deposition in the middle atmosphere. Part 1: Basic formulation. *J. Atm. Sol. Terr. Phys.*, *59*, 371-386.

Hohenegger, C., Kornblueh, L., Klocke, D., Becker, T., Cioni, G., Engels, J. F., ... Stevens, B. (2020). Climate statistics in global simulations of the atmosphere, from 80 to 2.5 km grid spacing. *Journal of the Meteorological Society of Japan. Ser. II*.

Huang, B., Thorne, P. W., Banzon, V. F., Boyer, T., Chepurin, G., Lawrimore, J. H., ... Zhang, H.-M. (2017). Extended reconstructed sea surface temperature, version 5 (ersstv5): upgrades, validations, and intercomparisons. *Journal of Climate*, *30*(20), 8179–8205.

Hurrell, J. W. (1995). Decadal trends in the north atlantic oscillation: Regional temperatures and precipitation. *Science*, *269*(5224), 676–679.

Hurtt, G., Chini, L., Sahajpal, R., Frolking, S., Bodirsky, B. L., Calvin, K., ... Zhang, X. (2019). *input4mips.cmip6.cmip.uofmd.uofmd-landstate-high-2-1-h.* Earth System Grid Federation. Retrieved from `https://doi.org/10.22033/ESGF/input4MIPs.11261` doi: 10.22033/ESGF/input4MIPs.11261

Ilyina, T., Six, K. D., Segschneider, J., Maier-Reimer, E., Li, H., & Núñez-Riboni, I. (2013). Global ocean biogeochemistry model hamocc: Model architecture and performance as component of the mpi-earth system model in different cmip5 experimental realizations. *Journal of Advances in Modeling Earth Systems*, *5*(2), 287–315.

Jochumsen, K., Quadfasel, D., Valdimarsson, H., & Jónsson, S. (2012). Variability of the Denmark Strait overflow: Moored time series from 1996–2011. *J. Geophys. Res.*, *117*, C12003. doi: 10.1029/2012JC008244

Johnson, G. C., Sloyan, B. M., Kessler, W. S., & McTaggart, K. E. (2002). Direct measurements of upper ocean currents and water properties across the tropical Pacific during the 1990s. *Progress in Oceanography*, *52*(1), 31–61.

Jungandreas, L., Hohenegger, C., & Claussen, M. (2021). Influence of the representation of convection on the mid-holocene west african monsoon. *Climate of the Past*, *17*, 1665–1684. doi: 10.5194/cp-17-1665-2021

Jungclaus, J. H., Fischer, N., Haak, H., Lohmann, K., Marotzke, J., Matei, D., ... von Storch, J. S. (2013). Characteristics of the ocean simulations in the Max Planck Institute Ocean Model (MPIOM) the ocean component of the MPI-Earth system model. *Journal of Advances in Modeling Earth Systems*, *5*(2), 422–446. doi: 10.1002/jame.20023

Kato, S., Rose, F. G., Rutan, D. A., Thorsen, T. J., Loeb, N. G., Doelling, D. R., ... Ham, S.-H. (2018). Surface irradiances of edition 4.0 clouds and the earth's radiant energy system (ceres) energy balanced and filled (ebaf) data product. *Journal of Climate*, *31*(11), 4501–4527.

Keeley, S. P. E., Sutton, R. T., & Shaffrey, L. C. (2012). The impact of North Atlantic sea surface temperature errors on the simulation of North Atlantic European region climate. *Quarterly Journal of the Royal Meteorological Society*, *138*(668), 1774–1783. doi: 10.1002/qj.1912

Kiladis, G. N., Wheeler, M. C., Haertel, P. T., Straub, K. H., & Roundy, P. E. (2009). Convectively coupled equatorial waves. *Reviews of Geophysics*, *47*(2).

Klocke, D., Brueck, M., Hohenegger, C., & Stevens, B. (2017). Rediscovery of the doldrums in storm-resolving simulations over the tropical atlantic. *Nature Geoscience*, *10*(12), 891–896.

Korn, P. (2017). Formulation of an unstructured grid model for global ocean dynamics. *Journal of Computational Physics*, *339*, 525–552. doi: 10.1016/j.jcp.2017.03.009

Korn, P. (2018). A Structure Preserving Discretization of Ocean Parametrizations on Unstructured Grids. *Ocean Modelling*, *132*, 73–90.

Korn, P., & Danilov, S. (2017). Elementary dispersion analysis of some mimetic discretizations on triangular c-grids. *Journal of Computational Physics*, *330*, 156–172. doi: 10.1016/j.jcp.2016.10.059

Korn, P., & Linardakis, L. (2018). A conservative discretization of the shallow-water equations on triangular grids. *Journal of Computational Physics*, *375*, 871–890.

Kwiatkowski, L., Torres, O., Bopp, L., Aumont, O., Chamberlain, M., Christian, J. R., ... others (2020). Twenty-first century ocean warming, acidification, deoxygenation, and upper-ocean nutrient and primary production decline from cmip6 model projections. *Biogeosciences*, *17*(13), 3439–3470.

Landschützer, P., Gruber, N., & Bakker, D. C. (2015). A 30 years observation-based global monthly gridded sea surface pco2 product from 1982 through 2011. *Carbon Dioxide Information Analysis Center, Oak Ridge National Laboratory, US Department of Energy, Oak Ridge, TN*.

Large, W. G., McWilliams, J. C., & Doney, S. C. (1994). Oceanic vertical mixing: A review and a model with a nonlocal boundary layer parameterization. *Reviews of geophysics*, *32*(4), 363–403.

Lenssen, N. J. L., Schmidt, G. A., Hansen, J. E., Menne, M. J., Persin, A., Ruedy, R., & Zyss, D. (2019). Improvements in the GISTEMP Uncertainty Model. *Journal of Geophysical Research-Atmospheres*, *124*(12), 6307–6326. doi: 10.1029/2018jd029522

Liu, X., & Schumaker, L. L. (1996). Hybrid bézier patches on sphere-like surfaces. *Journal of Computational and Applied Mathematics*, *73*(12), 157-172. doi: 10.1016/0377-0427(96)00041-6

Logemann, K., Linardakis, L., Korn, P., & Schrum, C. (2021). Global tide simulations with icon-o: testing the model performance on highly irregular meshes. *Ocean Dynamics*, *71*(1), 43–57.

Lohmann, K., Putrasahan, D., von Storch, J.-S., Gutjahr, O., Jungclaus, J. H., & Haak, H. (2021). Response of northern north atlantic and atlantic meridional overturning circulation to reduced and enhanced wind stress forcing. *Journal of Geophysical Research: Oceans*, *126*(11), e2021JC017902.

Lohmann, U., & Roeckner, E. (1996). Design and performance of a new cloud microphysics scheme developed for the echam general circulation model. *Climate Dynamics*, *12*(8), 557–572.

Lorenz, S., Jungclaus, J., Schmidt, H., Haak, H., Reick, C., Schupfner, M., ... Ilyina, T. (2021). *Mpi-m icon-esm-lr model output prepared for cmip6 cmip 1pctco2.* Earth System Grid Federation. Retrieved from `https://doi.org/10.22033/ESGF/CMIP6.6433` doi: 10.22033/ESGF/CMIP6.6433

Lott, F. (1999). Alleviation of stationary biases in a gcm through a mountain drag parameterization scheme and a simple representation of mountain lift forces. *Monthly weather review*, *127*(5), 788–801.

Maerz, J., Six, K. D., Stemmler, I., Ahmerkamp, S., & Ilyina, T. (2020). Microstructure and composition of marine aggregates as co-determinants for vertical particulate organic carbon transfer in the global ocean. *Biogeosciences*, *17*(7), 1765–1803.

Marshall, J., Scott, J. R., Romanou, A., Kelley, M., & Leboissetier, A. (2017). The dependence of the ocean's moc on mesoscale eddy diffusivities: A model study. *Ocean Modelling*, *111*, 1–8.

Marsland, S. J., Haak, H., Jungclaus, J. H., Latif, M., & Roske, F. (2003). The Max-Planck-Institute global ocean/sea ice model with orthogonal curvilinear coordinates. *Ocean Modelling*, *5*(2), 91–127. doi: 10.1016/S1463-5003(02)00015-X

Martin, J. H., Knauer, G. A., Karl, D. M., & Broenkow, W. W. (1987). Vertex: carbon cycling in the northeast pacific. *Deep Sea Research Part A. Oceanographic Research Papers*, *34*(2), 267–285.

Mauritsen, T., Bader, J., Becker, T., Behrens, J., Bittner, M., Brokopf, R., ... Roeckner, E. (2019). Developments in the MPI-M Earth System Model version 1.2 (MPI-ESM1.2) and Its Response to Increasing CO_2. *Journal of Advances in Modeling Earth Systems*, *11*(4), 998–1038. doi: 10.1029/2018ms001400

Mauritsen, T., & Roeckner, E. (2020). Tuning the MPI-ESM1.2 Global Climate Model to Improve the Match With Instrumental Record Warming by Lowering Its Climate Sensitivity. *Journal of Advances in Modeling Earth Systems*, *12*(5), e2019MS002037. doi: 10.1029/2019MS002037

Mauritsen, T., Stevens, B., Roeckner, E., Crueger, T., Esch, M., Giorgetta, M., ... Tomassini, L. (2012). Tuning the climate of a global model. *Journal of Advances in Modeling Earth Systems*, *4*, M00a01. doi: 10.1029/2012ms000154

Mauritsen, T., Svensson, G., Zilitinkevich, S. S., Esau, I., Enger, L., & Grisogono, B. (2007). A total turbulent energy closure model for neutrally and stably stratified atmospheric boundary layers. *Journal of Atmospheric Sciences*, *64*(11),

4113–4126.

Meehl, G. A., Senior, C. A., Eyring, V., Flato, G., Lamarque, J.-F., Stouffer, R. J., ... Schlund, M. (2020). Context for interpreting equilibrium climate sensitivity and transient climate response from the CMIP6 Earth system models. *Science Advances*, *6*(26), eaba1981. doi: 10.1126/sciadv.aba1981

Mehlmann, C., Danilov, S., Losch, M., Lemieux, J.-F., Hutter, N., Richter, T., ... Korn, P. (2021). Simulating linear kinematic features in viscous-plastic sea ice models on quadrilateral and triangular grids with different variable staggering. *Journal of Advances in Modeling Earth Systems*, *13*(11), e2021MS002523.

Mehlmann, C., & Korn, P. (2021). Sea-ice dynamics on triangular grids. *Journal of Computational Physics*, *428*, 110086.

Milinski, S., Bader, J., Haak, H., Siongco, A. C., & Jungclaus, J. H. (2016). High atmospheric horizontal resolution eliminates the wind-driven coastal warm bias in the southeastern tropical Atlantic. *Geophysical Research Letters*, *43*(19), 10455–10462. doi: 10.1002/2016gl070530

Morice, C. P., Kennedy, J. J., Rayner, N. A., & Jones, P. D. (2012). Quantifying uncertainties in global and regional temperature change using an ensemble of observational estimates: The HadCRUT4 data set. *Journal of Geophysical Research-Atmospheres*, *117*, D08101. doi: 10.1029/2011jd017187

Müller, W. A., Jungclaus, J. H., Mauritsen, T., Baehr, J., Bittner, M., Budich, R., ... Marotzke, J. (2018). A Higher-resolution Version of the Max Planck Institute Earth System Model (MPI-ESM1.2-HR). *Journal of Advances in Modeling Earth Systems*, *10*(7), 1383–1413. doi: 10.1029/2017ms001217

Nabel, J. E., Naudts, K., & Pongratz, J. (2020, jan). Accounting for forest age in the tile-based dynamic global vegetation model JSBACH4 (4.20p7; git feature/forests) - a land surface model for the ICON-ESM. *Geoscientific Model Development*, *13*(1), 185–200. doi: 10.5194/gmd-13-185-2020

Nam, C., Bony, S., Dufresne, J.-L., & Chepfer, H. (2012). The 'too few, too bright'tropical low-cloud problem in cmip5 models. *Geophysical Research Letters*, *39*(21).

Nordeng, T.-E. (1994, 09). *Extended versions of the convective parametrization scheme at ecmwf and their impact on the mean and transient activity of the model in the tropics* (No. 206). Shinfield Park, Reading: ECMWF. Retrieved from `https://www.ecmwf.int/node/11393` doi: 10.21957/e34xwhysw

Notz, D. (2020). Simip community, 2020: Arctic sea ice in cmip6. *Geophys. Res. Lett*, *47*, e2019GL086749.

Notz, D., Haumann, F. A., Haak, H., Jungclaus, J. H., & Marotzke, J. (2013). Arctic sea-ice evolution as modeled by max planck institute for meteorology's earth system model. *Journal of Advances in Modeling Earth Systems*, *5*(2), 173–194.

Nowlin Jr., W. D., & Klinck, J. M. (1986). The physics of the Antarctic Circumpolar Current. *Rev. Geophys.*, *24(3)*, 469–491. doi: 10.1029/RG024i003p00469

Olbers, D., & Eden, C. (2013). A Global Model for the Diapycnal Diffusivity Induced by Internal Gravity Waves. *J. Phys. Oceanogr.*, *43*(8), 1759–1779. doi: 10.1175/JPO-D-12-0207.1

Olsen, A., Key, R. M., Van Heuven, S., Lauvset, S. K., Velo, A., Lin, X., ... others (2016). The global ocean data analysis project version 2 (glodapv2)–an internally consistent data product for the world ocean. *Earth System Science Data*, *8*(2), 297–323.

Pacanowski, R. C., & Philander, S. G. H. (1981). Parameterization of vertical mixing in numerical models of tropical oceans. *Journal of Physical Oceanography*, *11*(11), 1443–1451. doi: 10.1175/1520-0485(1981)011⟨1443:POVMIN⟩2.0.CO;2

Paulsen, H., Ilyina, T., Six, K. D., & Stemmler, I. (2017). Incorporating a prognostic representation of marine nitrogen fixers into the global ocean biogeochemical

model hamocc. *Journal of Advances in Modeling Earth Systems*, *9*(1), 438–464.

Petersen, M. R., Asay-Davis, X. S., Berres, A. S., Chen, Q., Feige, N., Hoffman, M. J., ... Woodring, J. L. (2019). An evaluation of the ocean and sea ice climate of e3sm using MPAS and interannual CORE-II forcing. *Journal of Advances in Modeling Earth Systems*, *11*(5), 1438–1458. doi: 10.1029/2018ms001373

Phillips, A. S., Deser, C., & Fasullo, J. (2014). Evaluating modes of variability in climate models. *Eos, Transactions American Geophysical Union*, *95*(49), 453–455. doi: 10.1002/2014EO490002

Pincus, R., & Stevens, B. (2013). Paths to accuracy for radiation parameterizations in atmospheric models. *Journal of Advances in Modeling Earth Systems*, *5*(2), 225–233.

Pongratz, J., Reick, C., Raddatz, T., & Claussen, M. (2008). A reconstruction of global agricultural areas and land cover for the last millennium. *Global Biogeochemical Cycles*, *22*(3). doi: 10.1029/2007GB003153

Putrasahan, D. A., Lohmann, K., von Storch, J. S., Jungclaus, J. H., Gutjahr, O., & Haak, H. (2019). Surface Flux Drivers for the Slowdown of the Atlantic Meridional Overturning Circulation in a High-Resolution Global Coupled Climate Model. *Journal of Advances in Modeling Earth Systems*, *11*(5), 1349–1363. doi: 10.1029/2018ms001447

Rayner, N., Parker, D. E., Horton, E., Folland, C. K., Alexander, L. V., Rowell, D., ... Kaplan, A. (2003). Global analyses of sea surface temperature, sea ice, and night marine air temperature since the late nineteenth century. *Journal of Geophysical Research: Atmospheres*, *108*(D14).

Redi, M. (1982). Oceanic Isopycnal Mixing by Coordinate Rotation [Journal Article]. *Journal of Physical Oceanography*, *12*, 1154–1158.

Reichler, T., & Kim, J. (2008). How well do coupled models simulate today's climate? *Bulletin of the American Meteorological Society*, *89*(3), 303–312.

Reick, C. H., Gayler, V., Goll, D., Hagemann, S., Heidkamp, M., Nabel, J. E. M. S., ... Wilkenskjeld, S. (2021). JSBACH 3 - The land component of the MPI Earth System Model: Documentation of version 3.2. *Berichte zur Erdsystemforschung*, *240*. doi: 10.17617/2.3279802

Reick, C. H., Raddatz, T., Brovkin, V., & Gayler, V. (2013). Representation of natural and anthropogenic land cover change in MPI-ESM. *Journal of Advances in Modeling Earth Systems*, *5*(3), 459–482. doi: 10.1002/jame.20022

Riddick, T. (2021). *Generation of hd parameters files for icon grids: technical note.* doi: 10.17617/2.3336390

Rieger, D., Bangert, M., Bischoff-Gauss, I., Förstner, J., Lundgren, K., Reinert, D., ... others (2015). Icon–art 1.0–a new online-coupled model system from the global to regional scale. *Geoscientific Model Development*, *8*(6), 1659–1676.

Roeckner, E., Bäuml, G., Bonaventura, L., Brokopf, R., Esch, M., Giorgetta, M., ... Tompkins, A. (2003). *The atmospheric general circulation model ECHAM 5. PART I: Model description* (Vol. 349). Hamburg: Max-Planck-Institut für Meteorologie. Retrieved from `https://pure.mpg.de/pubman/item/item_995269_6/component/file_3192562/349-Report-txt.pdf` doi: 10.17617/2.995269

Rossby, T., & Flagg, C. (2012). Direct measurement of volume flux in the Faroe-Shetland Channel and over the Iceland-Faroe Ridge. *Geophys. Res. Lett.*, *39*, L07602. doi: 10.1029/2012GL051269

Satoh, M., Tomita, H., Yashiro, H., Miura, H., Kodama, C., Seiki, T., ... others (2014). The non-hydrostatic icosahedral atmospheric model: Description and development. *Progress in Earth and Planetary Science*, *1*(1), 1–32.

Schaaf, C., & Wang, Z. (2015). MCD43C3 MODIS/Terra+ Aqua BRDF/Albedo Albedo Daily L3 Global 0.05 Deg CMG V006. *NASA EOSDIS Land Processes*

DAAC. doi, *10*. doi: doi.org/10.5067/MODIS/MCD43C3.006

Schaaf, C. B., Gao, F., Strahler, A. H., Lucht, W., Li, X., Tsang, T., ... others (2002). First operational BRDF, albedo nadir reflectance products from MODIS. *Remote sensing of Environment*, *83*(1-2), 135–148. doi: 10.1016/S0034-4257(02)00091-3

Scholz, P., Sidorenko, D., Gurses, O., Danilov, S., Koldunov, N., Wang, Q., ... Jung, T. (2019). Assessment of the finite-volumE sea ice-ocean model (FESOM2.0) – part 1: Description of selected key model elements and comparison to its predecessor version. *Geoscientific Model Development*, *12*(11), 4875–4899. doi: 10.5194/gmd-12-4875-2019

Séférian, R., Berthet, S., Yool, A., Palmieri, J., Bopp, L., Tagliabue, A., ... others (2020). Tracking improvement in simulated marine biogeochemistry between cmip5 and cmip6. *Current Climate Change Reports*, 1–25.

Sein, D. V., Koldunov, N. V., Danilov, S., Wang, Q., Sidorenko, D., Fast, I., ... Jung, T. (2017). Ocean modeling on a mesh with resolution following the local rossby radius. *Journal of Advances in Modeling Earth Systems*, *9*(7), 2601–2614. doi: 10.1002/2017ms001099

Semmler, T., Danilov, S., Gierz, P., Goessling, H. F., Hegewald, J., Hinrichs, C., ... Jung, T. (2020). Simulations for CMIP6 with the AWI climate model AWI-CM-1-1. *Journal of Advances in Modeling Earth Systems*, *12*(9). doi: 10.1029/2019ms002009

Semmler, T., Jungclaus, J., Danek, C., Goessling, H. F., Koldunov, N., Rackow, T., & Sidorenko, D. (2021). Ocean model formulation influences transient climate response. *Journal of Geophysical Research: Oceans*, e2021JC017633.

Semtner, A. (1976). A model for the thermodynamic growth of sea ice in numerical investigations of climate. *Journal of Physical Oceanography*, *6*, 379–389.

Sherwood, S., Webb, M. J., Annan, J. D., Armour, K., Forster, P. M., Hargreaves, J. C., ... others (2020). An assessment of earth's climate sensitivity using multiple lines of evidence. *Reviews of Geophysics*, *58*(4), e2019RG000678.

Six, K. D., & Maier-Reimer, E. (1996). Effects of plankton dynamics on seasonal carbon fluxes in an ocean general circulation model. *Global Biogeochemical Cycles*, *10*(4), 559–583.

Skamarock, W. C., Klemp, J. B., Duda, M. G., Fowler, L. D., Park, S.-H., & Ringler, T. D. (2012). A multiscale nonhydrostatic atmospheric model using centroidal voronoi tesselations and c-grid staggering. *Monthly Weather Review*, *140*(9), 3090–3105. doi: 10.1175/mwr-d-11-00215.1

Smeed, D. A., Josey, S. A., Beaulieu, C., Johns, W. E., Moat, B. I., Frajka-Williams, E., ... McCarthy, G. D. (2018). The North Atlantic Ocean Is in a State of Reduced Overturning. *Geophysical Research Letters*, *45*(3), 1527–1533. doi: 10.1002/2017gl076350

Smith, T. M., Reynolds, R. W., Peterson, T. C., & Lawrimore, J. (2008). Improvements to NOAA's historical merged land–ocean surface temperature analysis (1880–2006). *Journal of Climate*, *21*(10), 2283–2296. doi: 10.1175/2007JCLI2100.1

Staniforth, A., & Thuburn, J. (2011, November). Horizontal grids for global weather and climate prediction models: a review. *Quarterly Journal of the Royal Meteorological Society*, *138*(662), 1–26. doi: 10.1002/qj.958

Steele, M., Morley, R., & Ermold, W. (2001). PHC: A global ocean hydrography with a high-quality Arctic Ocean. *Journal of Climate*, *14*(9), 2079–2087. doi: Doi10.1175/1520-0442(2001)014⟨2079:Pagohw⟩2.0.Co;2

Stevens, B., Giorgetta, M., Esch, M., Mauritsen, T., Crueger, T., Rast, S., ... Roeckner, E. (2013). Atmospheric component of the MPI-M Earth System Model: ECHAM6. *Journal of Advances in Modeling Earth Systems*, *5*(2), 146–172. doi: 10.1002/jame.20015

Stevens, B., Satoh, M., Auger, L., Biercamp, J., Bretherton, C. S., Chen, X., ...

others (2019). Dyamond: the dynamics of the atmospheric general circulation modeled on non-hydrostatic domains. *Progress in Earth and Planetary Science*, *6*(1), 1–17.

Sundqvist, H., Berge, E., & KRISTJANSSON, J. (1989). Condensation and cloud parameterization studies with a mesoscale numerical weather prediction model. *Monthly Weather Review*, *117*(8), 1641–1657.

Talley, L. D., Reid, J. L., & Robbins, P. E. (2003). Data-based meridional overturning streamfunctions for the global ocean. *Journal of Climate*, *16*(19), 3213–3226. doi: Doi10.1175/1520-0442(2003)016⟨3213:Dmosft⟩2.0.Co;2

Tian, B., & Dong, X. (2020). The double-itcz bias in cmip3, cmip5, and cmip6 models based on annual mean precipitation. *Geophysical Research Letters*, *47*(8), e2020GL087232.

Tiedtke, M. (1989). A comprehensive mass flux scheme for cumulus parameterization in large-scale models. *Monthly weather review*, *117*(8), 1779–1800.

Tomita, H., Satoh, M., & Goto, K. (2002). An optimization of the icosahedral grid modified by spring dynamics. *Journal of Computational Physics*, *183*(1), 307–331.

Tomita, H., Tsugawa, M., Satoh, M., & Goto, K. (2001). Shallow water model on a modified icosahedral geodesic grid by using spring dynamics. *Journal of Computational Physics*, *174*(2), 579–613.

Ullrich, P. A., Jablonowski, C., Kent, J., Lauritzen, P. H., Nair, R., Reed, K. A., ... Viner, K. (2017). DCMIP2016: a review of non-hydrostatic dynamical core design and intercomparison of participating models. *Geoscientific Model Development*, *10*(12), 4477–4509. doi: 10.5194/gmd-10-4477-2017

Van Roekel, L., Adcroft, A. J., Danabasoglu, G., Griffies, S. M., Kauffman, B., Large, W., ... Schmidt, M. (2018). The KPP Boundary Layer Scheme for the Ocean: Revisiting Its Formulation and Benchmarking One-Dimensional Simulations Relative to LES. *Adv. Model. Earth Syst.*, *10*(11), 2647–2685. doi: 10.1029/2018MS001336

Wan, H., Giorgetta, M. A., Zängl, G., Restelli, M., Majewski, D., Bonaventura, L., ... others (2013). The icon-1.2 hydrostatic atmospheric dynamical core on triangular grids–part 1: Formulation and performance of the baseline version. *Geoscientific Model Development*, *6*(3), 735–763.

Wan, Z., Hook, S., & Hulley, G. (2015). *Mod11c1 modis/terra land surface temperature/emissivity daily l3 global 0.05deg cmg v006 data set.* distributed in netCDF format by the Integrated Climate Data Center (ICDC, icdc.cen.uni-hamburg.de) University of Hamburg, Hamburg, Germany. (last access date: January 6 2020)

Wedi, N. P. (2014). Increasing horizontal resolution in numerical weather prediction and climate simulations: illusion or panacea? *Philosophical Transactions of the Royal Society A: Mathematical, Physical and Engineering Sciences*, *372*(2018), 20130289. doi: 10.1098/rsta.2013.0289

Weller, H., Weller, H. G., & Fournier, A. (2009). Voronoi, delaunay, and block-structured mesh refinement for solution of the shallow-water equations on the sphere. *Monthly weather review*, *137*(12), 4208–4224.

Wheeler, M., & Kiladis, G. N. (1999). Convectively coupled equatorial waves: Analysis of clouds and temperature in the wavenumber–frequency domain. *Journal of Atmospheric Sciences*, *56*(3), 374–399.

Wieners, K.-H., Giorgetta, M., Jungclaus, J., Reick, C., Esch, M., Bittner, M., ... Roeckner, E. (2019). *Mpi-m mpi-esm1.2-lr model output prepared for cmip6 cmip historical.* Earth System Grid Federation. Retrieved from `https://doi.org/10.22033/ESGF/CMIP6.6595` doi: 10.22033/ESGF/CMIP6.6595

Woodgate, R. A., Aagard, K., & Weingartner, T. J. (2006). Interannual changes in the Bering Strait fluxes of volume, heat, and freshwater between 1991 and 2004. *Geophys. Res. Lett.*, *33*, L15609. doi: 10.1029/2006GL026931

Woodgate, R. A., Weingartner, T., & Lindsa, R. (2012). Observed increases in Bering Strait oceanic fluxes from the Pacific to the Arctic from 2001 to 2011 and their impacts on the Arctic Ocean water column. *Geophys. Res. Lett.*, *39*, L24603. doi: 10.1029/2012GL054092

Zängl, G., Reinert, D., Ripodas, P., & Baldauf, M. (2015). The ICON (ICOsahedral Non-hydrostatic) modelling framework of DWD and MPI-M: Description of the non-hydrostatic dynamical core. *Quarterly Journal of the Royal Meteorological Society*, *141*(687), 563–579. doi: 10.1002/qj.2378

Zhang, H.-M., Lawrimore, J. H., Huang, B., Menne, M. J., Yin, X., Sánchez-Lugo, A., ... Williams, C. N. (2019). Updated temperature data give a sharper view of climate trends. *Eos, Trans. Amer. Geophys. Union*, *100*. doi: 10.1029/2019EO128229